

A simple, stable, and accurate tetrahedral finite element for transient, nearly incompressible, linear and nonlinear elasticity: A dynamic variational multiscale approach.

Journal:	<i>International Journal for Numerical Methods in Engineering</i>
Manuscript ID:	NME-May-15-0302
Wiley - Manuscript type:	Research Article
Date Submitted by the Author:	04-May-2015
Complete List of Authors:	Scovazzi, Guglielmo; Duke University, Civil & Environmental Carnes, Brian; Sandia National Laboratories, Advanced Computational Mechanics Architectures Zeng, Xianyi; Duke University, Civil & Environmental Department
Keywords:	Elasticity, Finite element methods, Nonlinear dynamics, Solids, Lagrangian, Time integration, Explicit

SCHOLARONE™
Manuscripts

INTERNATIONAL JOURNAL FOR NUMERICAL METHODS IN ENGINEERING

Int. J. Numer. Meth. Engng 2014; **00**:1–40

Published online in Wiley InterScience (www.interscience.wiley.com). DOI: 10.1002/nme

A simple, stable, and accurate tetrahedral finite element for transient, nearly incompressible, linear and nonlinear elasticity: A dynamic variational multiscale approach

G. Scovazzi^{†*}, B. Carnes[‡], X. Zeng[†][†]*Department of Civil & Environmental Engineering, Duke University, Room 121 Hudson Hall, P.O. Box 90287, Durham, NC 27708-0287, USA*[‡]*Validation and Uncertainty Quantification Department, Sandia National Laboratories, P.O. Box 5800, MS 0382, Albuquerque, NM 87185-0382, USA*

SUMMARY

We propose a new approach for the stabilization of simple linear tetrahedral finite elements in the case of nearly incompressible transient solid dynamics computations. Our method is based on a mixed formulation, in which the momentum equation is complemented by a rate equation for the evolution of the pressure field, approximated with piecewise linear, continuous finite element functions. The pressure equation is stabilized to prevent spurious pressure oscillations in computations. Incidentally, it is also shown that many stabilized methods previously developed for the static case do not generalize easily to transient dynamics. Extensive tests in the context of linear and nonlinear elasticity are used to corroborate the claim that the proposed method is robust, stable and accurate. Copyright © 2014 John Wiley & Sons, Ltd.

Received ...

KEY WORDS: Tetrahedral finite element; piece-wise linear interpolation; stabilized method; transient dynamics; nearly incompressible elasticity

1. INTRODUCTION

Modern computational mechanics applications are often characterized by complex geometry. There might be different reasons for the geometrical complexity of designs: The use of automated optimization techniques, which may select non-intuitive shapes as the final concept, or a deeper understanding about the physical phenomena involved, which may spur engineers towards extreme design choices, etc. Biomechanics, bioengineering, and geomechanics are becoming prominent examples in the realm of applications with complex geometry in addition to the fields of civil, mechanical, and aerospace engineering.

Many of the applications considered above involve incompressible or nearly incompressible materials. For example, many biological materials, a large number of polymeric compounds (including most rubbers), and certain types of soils and geologic strata can be modeled as nearly incompressible.

An additional element of complexity considered in this work is the simulation of time dependent problems, which may pose specific challenges to methods initially developed for static computations.

*Correspondence to: Guglielmo Scovazzi (guglielmo.scovazzi@duke.edu), Department of Civil & Environmental Engineering, Duke University, Room 121 Hudson Hall, P.O. Box 90287, Durham, NC 27708-0287, USA

When considering nearly or fully incompressible materials, a number of well established computational methods are available. If simplicity of implementation is the goal, selective reduced integration methods are the standard in the field. Many variants can be considered, such as the B-bar [1–3] or F-bar [4–6] methods, or the mean dilatation finite element method [7]. These approaches avoid volumetric locking [1] by reducing the total number of discrete incompressibility constraints evaluated at quadrature points. Fundamentally, these elements circumvent the restrictions associated with the Ladyzhenskaya-Babuška-Brezzi (LBB) conditions [8–10] (also known as *inf-sup* conditions).

One peculiarity of the approaches just described is that they are tailored to unstructured quadrilateral finite elements in two dimensions and unstructured hexahedral elements in three dimensions. Unfortunately, the automated generation of hexahedral grids in complex geometry is in many respects an open problem to date. In fact, hexahedral grid generation is labor intensive, and requires times that are one order of magnitude larger than the actual computing time. A number of new ideas are being developed for advanced hexahedral meshing: They typically involve an octree-type strategy for the bulk of the computational domain, and heterogeneous meshing using wedge, pyramid and more general polygonal elements near the boundaries of the computational domain. Although heterogeneous grids that are mostly constituted of hexahedral elements can be automatically generated, these tend to suffer from distortion near boundaries, where mesh quality is often paramount, and necessitate generalized polygonal finite element methods, which are still object of intense research development.

The meshing bottleneck just described can be addressed by employing triangular and tetrahedral grids in two and three dimensions respectively. In fact, automated Delaunay and advancing front algorithms are a mature, robust technology, of widespread use in commercial software. In particular, it is a fair assessment to say that tetrahedral mesh generation times are of the same order of computational run-times. However, a problematic issue is that there are no simple tetrahedral finite element formulations that are robust and accurate, particularly in the time-dependent, nearly or fully incompressible cases. Current available methods typically suffer from rather complicated implementations, and, in some cases, lack of stability/robustness. Another aspect worth of notice is the scarcity, in the published literature, of developments in the context of transient dynamics, as most of the contributions pertain to static computations. Observing that the equations of static elasticity are elliptic, while the equations of elastodynamics lead to a hyperbolic system, it becomes clear that this change in structure cannot be overlooked when designing effective computational methods. We will show in particular that some of the previous strategies based on enrichment bubbles or stabilized methods for static problems do not generalize appropriately to the time-dependent case.

We provide next a very brief account of recent developments in tetrahedral finite elements in nearly and fully incompressible elasticity. Computing on tetrahedral finite elements of simple type was an area of active research as early as the beginnings of the finite element method. However, volumetric locking in the incompressible limit prevented the use of displacement based formulations in conjunction with linear interpolation. At the time, the work of Malkus and Hughes [11] was very instrumental in explaining that displacement-based linear finite elements on tetrahedral grids are equivalent to mixed finite elements in which the stresses are approximated by piecewise constant fields over the elements (constant strain tetrahedral elements). This seminal work made the connection between reduced order integration and mixed finite element interpolations, and helped improve the understanding of volumetric locking in displacement-based formulations from the perspective of the LBB conditions.

Almost a decade later, in the context of fluid mechanics, a number of advances were been made in stabilized finite element methods for the Stokes and Navier-Stokes equations. In particular, in [12–14], a new form of stabilization was proposed to obtain a simple finite element formulation of the Stokes flow problem in combination with piecewise linear interpolation for the velocity/pressure pair. The proposed stabilization prevented spurious node-to-node pressure oscillations, detected in previous computational experiments. Observing that the equations of stationary Stokes flow are formally identical to the equations of static incompressible elasticity, Hughes, Franca, and

collaborators [13, 15] proposed to extend to the latter the approach initially pursued in [12]: In what follows, we will indicate with HFB this method.

In the years to follow, an extension of the HFB approach to nonlinear elastic-visco-plastic static computations was pursued by the group of Maniatty [16–20]. More recently, Masud and co-authors pursued implementations of the stabilized approach by means of bubble functions, with the purpose of avoiding any tunable parameters in computations [21–23]. Very recently, Masud and Truster [24] extended to nonlinear hyper-elasticity these strategies by means of the variational multiscale framework [25–27]. In parallel to these developments, Chiumenti and co-authors [28–30] attacked problems in incompressible nonlinear elasticity and elastoplasticity using the orthogonal subscales (OSS) method, a variant of the stabilized method in [12] introduced by Codina [31].

As these developments were taking place, a number of researchers started to independently develop mixed finite element methods with nodal finite element spaces for the strains/stresses. These formulations produce a considerable increase in the number of unknowns per node, but the nodal storage somewhat alleviates the total increase in global unknowns, since for a typical tetrahedral grid, the number of nodes is about 5–7 times lower than the number of elements. If nodal strains are used in place of nodal stresses, then the evaluation of constitutive models (often times a large component to the computational burden in nonlinear problems) occurs at the nodes, and a further reduction in the computational cost can be achieved. Another reason why nodal linear approximations for the stress tensor are pursued is that, at least in principle, they can be second order accurate. We caution the reader here that the convergence rates do not exclusively depend on the order of interpolation, but also on the optimality of the numerical method adopted. The averaged nodal stress element of Bonet and collaborators [32, 33] was one of the earliest attempts of this type in the realm of transient dynamics. The work of Puso and Solberg [34] proposed to blend the constant and nodal strain finite elements with the goal of avoiding locking, and the work of Dormann, Gee, and collaborators [35, 36] explored the idea of averaging the deviator of the strain, to improve bending performance. Fundamentally, however, all the mentioned nodal strain or nodal stress elements did not satisfy the LBB condition, as Stenberg [37] pointed out just a few years earlier, in the linear case. Cervera and collaborators [38–43] explored then the idea of stabilizing the tensor of nodal stresses, using the variational multiscale approach and the OSS method, and focusing predominantly on static problems.

Over the past couple of years, Bonet, Gil and collaborators published a number of works [44–47], in which a new first-order (mixed) form of the equations of nonlinear solid mechanics was pursued. This approach is very promising and it is the first of its kind in the context of Lagrangian frames, since earlier work of Trangenstein and co-authors [48–51] was limited to Eulerian reference frames. Features of the proposed framework [44–47] are the use, as an additional variable, of a nodally interpolated deformation gradient \mathbf{F} (a non-symmetric tensor), and Lagrange multipliers to enforce conservation of angular momentum, whenever deemed important in computations. In addition, test reported in [44–47] showed second-order convergence for the stresses. In the incompressible limit, it was found necessary to introduce as an additional nodal variable the Jacobian determinant of the deformation gradient (J) [52–54]. In very recent work, Bonet and co-authors [52] developed a systematic approach to define entropy variable/flux pairs for polyconvex constitutive models, by introducing a nodal cofactor tensor ($\text{cof } \mathbf{F}$) as an additional nodal unknown. Methods based on nodal interpolations of \mathbf{F} , J , or $\text{cof } \mathbf{F}$ are inherently unstable, and for this reason the authors in [45–47] introduced stabilizing mechanisms through a combination of the SUPG stabilization [55–65], and penalties on the difference between the nodal and standard (constant) approximation of the deformation gradient (in analogy to Puso and Solberg [34]). Alternatively, Aguirre and collaborators [44, 66] pursued stability by means of approximate Riemann solvers for nodal finite volumes.

There are at least seven other classes of methods that have been proposed over the years: 1) Zienkiewicz, Pastor and collaborators [67–71] proposed the idea of using Chorin's pressure projection method to obtain simple finite element formulations to tackle the incompressible limit, with some time dependent examples. Pressure projection for nodal elements was explored in fluid mechanics at about the same time by Guermond and Quartapelle [72], who showed that Chorin's

approach, *per se*, cannot resolve the numerical instabilities of the finite element formulations to which it is applied. 2) Oñate [73, 74] suggested a stabilized method based on the finite calculus framework, ultimately very similar to [13, 14]. 3) Guo, Thoutireddy and collaborators proposed the idea of composite elements [75, 76], in which internal degrees of freedom for the velocity are created through a local subdivision of each element of the mesh. This last method bears some similarities with stabilized methods based on bubbles, and also in this case computations were limited to the static case. 4) Important contributions are also the ones of de Souza Neto and collaborators [4–6, 77], which developed the F-bar strategy to stabilize nonlinear finite element computations on tetrahedra. These methods rely on finding appropriate element patches to compute an average of the deformation gradient, and reducing the number of discrete incompressibility constraints enforced. The F-bar approach to tetrahedral finite elements showed great promise, although again the computations were limited to static problems, and the implementation required more involved data structures. 5) Very recently, Lew and collaborators [78–81] proposed and proved stability for a discontinuous Galerkin (DG) method applicable to general grids (hence tetrahedral elements) in the static case. DG methods typically involve increased computational cost in the case of low-order approximations - particularly in three dimensions - and a new hybridizable DG method was proposed in [82] to address this issue. 6) As an alternative to the methods mentioned so far, Taylor and Kasper [83–85] attacked the problem of stable computations on simple tetrahedral finite elements resorting to two- and three-field mixed problems. These approaches inherently produce a very large number of unknowns, some of which can be statically condensed, since they are local to elements. These developments were also limited to static problems, and in that case it was possible to derive stability proofs [86]. 7) More recently, Arnold, Falk and Winther developed a framework for elasticity based on compatible discretizations [87–90], defining a complex for the linear elasticity differential operators analogous to the de Rham complex in electromagnetism [91]. The result of these developments are provably stable elements for static problems, which however involve mixed formulations with larger number of unknowns.

Our approach has been under development since late 2011, and aims at attaining robust and accurate computations in the nearly and fully incompressible cases, with a new tetrahedral finite element with computational cost and ease of implementation comparable to the constant strain/linear displacement tetrahedral finite element. Fundamentally, we use a mixed form of the variational problem, in terms of the displacement and pressure fields, both approximated with piecewise linear functions.

Initially we attempted at developing simple extensions of the HFB approach to time-dependent problems, but we observed in computational experiments that the resulting methods could not achieve robustness and reliability. We in fact realized that the hyperbolic structure of the time-dependent solid mechanics problems could not be captured by the stabilizing operators developed in [13, 14], for the elliptic equations of static linear elasticity. In simple terms, the methods detailed in [13, 14] rely on the residual of the equilibrium balance to stabilize the incompressibility constraint equation. If the same methods were to be used in the time dependent case, that would amount to stabilize the pressure equation (or the incompressibility constraint equation) with a single time-snapshot of the residual. In our analysis, we will show that this approach is not sufficient, in that it leads to catastrophic algorithmic failures in very simple standardized tests.

To overcome these critical issues, we propose to build stabilization terms that somehow track the history of the residual over time, inspired by previous work of the first of the authors in the context of nodal-based Lagrangian shock hydrodynamics finite element computations [92]. We propose a simple approach to achieve this goal, which is to resort to a pressure update equation in rate form, and to build stabilizing mechanism within that context.

The resulting method is very simple, since only one scalar equation (for the pressure unknown) is required in addition to the momentum balance (and displacement unknowns). We show with an extensive number of computations that the proposed method is accurate, robust, and that its performance closely matches the B-bar hexahedral element over grids of similar resolution. As such, the proposed method could be a valuable candidate for large-scale computations on geometrically complex unstructured tetrahedral grids.

The remainder of this paper is organized as follows: in Section 2, the problem of interest is stated, including governing equations, constitutive laws, and initial and boundary conditions; in Section 3 the proposed stabilized method is presented for linearly elastic materials, and corresponding numerical results are shown in Section 4; an extension to nonlinear hyper-elasticity is considered in Section 5, and its numerical performance is assessed by extensive tests in Section 6; finally, conclusions and future directions are summarized in Section 7.

2. STATEMENT OF THE PROBLEM

In this work we consider problems in linear (small strain) and nonlinear (finite strain) elasticity. We will pose problems using the Lagrangian mechanics formalism, with the following notation conventions: regular fonts, such as t , p , and ρ , denote a scalar (variable or function), while bold fonts, such as \mathbf{x} , \mathbf{b} , and $\boldsymbol{\varphi}$, designate vector or tensor quantities.

2.1. Governing equations

The equations of Lagrangian solid dynamics govern the rate of change of position, density, and momentum, for a body of material as it deforms. The initial and current configurations of the body are denoted by Ω_0 and Ω , respectively, two open sets in \mathbb{R}^{n_d} with Lipschitz boundaries ($n_d = 2, 3$ indicates the number of spatial dimensions). The deformation of the body is characterized by the *motion*

$$\boldsymbol{\varphi} : \Omega_0 \rightarrow \Omega = \boldsymbol{\varphi}(\Omega_0) , \quad (1a)$$

$$\mathbf{X} \mapsto \mathbf{x} = \boldsymbol{\varphi}(\mathbf{X}, t) , \quad \forall \mathbf{X} \in \Omega_0, t \geq 0 , \quad (1b)$$

which maps the material coordinate \mathbf{X} , representing the initial position of an infinitesimal material particle of the body, to \mathbf{x} , the position of the same particle in the current configuration. We denote the boundaries of these domains by $\Gamma_0 = \partial\Omega_0$ and $\Gamma = \partial\Omega$, and always assume that $\boldsymbol{\varphi}(\Gamma_0) = \Gamma$. We also assume that $\boldsymbol{\varphi}$ is smooth and invertible, such that the *deformation gradient* $\mathbf{F} = \nabla_{\mathbf{X}}\boldsymbol{\varphi}$ and the *deformation Jacobian determinant* $J = \det \mathbf{F} > 0$ are always well defined.

Denoting by ρ , $\mathbf{u} = \mathbf{x} - \mathbf{X}$, and \mathbf{v} the density, displacement, and velocity, respectively, the governing equations of the solid dynamics problem are:

$$\dot{\mathbf{u}} = \mathbf{v} , \quad (2a)$$

$$\rho J = \rho_0 , \quad (2b)$$

$$\rho \dot{\mathbf{v}} = \rho \mathbf{b} + \nabla_{\mathbf{x}} \cdot \boldsymbol{\sigma} . \quad (2c)$$

Here ρ_0 is the initial density, \mathbf{b} is the body force, $\boldsymbol{\sigma}$ is the symmetric Cauchy stress tensor, and $\nabla_{\mathbf{x}}$ and $\nabla_{\mathbf{x}} \cdot$ are the current configuration gradient and divergence operators, respectively. In addition, $\dot{\mathbf{u}}$ and $\dot{\mathbf{v}}$ designate the material (or Lagrangian) time derivatives of the displacement and velocity vectors (namely, $\dot{\mathbf{u}} = \partial_t \mathbf{u}|_{\mathbf{X}}$ and $\dot{\mathbf{v}} = \partial_t \mathbf{v}|_{\mathbf{X}}$). The set of equations (2) completely define the evolution of the system, once a constitutive relationship for the stress $\boldsymbol{\sigma}$ is specified, together with appropriate initial and boundary conditions.

2.2. Isotropic materials with hydrostatic/deviatoric split of the stress tensor

In this work, we consider isotropic materials, whose constitutive laws allow for a decomposition of the stress into an hydrostatic (pressure) and deviatoric components, as

$$\boldsymbol{\sigma} = p\mathbf{I} + \text{dev}[\boldsymbol{\sigma}] , \quad (3)$$

where \mathbf{I} is the unit tensor in $\mathbb{R}^{n_d \times n_d}$, with Cartesian components given by the Kronecker symbol δ_{ij} (we recall that $\delta_{ij} = 1$ if $i = j$ and 0 if otherwise), an . In equation (3), $p = 1/3 \sigma_{kk}$ indicates the pressure, and $\text{dev}[\boldsymbol{\sigma}]$ the deviator of the stress, expressed in index notation as $\text{dev}[\boldsymbol{\sigma}]_{ij} = \sigma_{ij} -$

$p\delta_{ij} = \sigma_{ij} - 1/3 \sigma_{kk}$. This decomposition is particularly useful for nearly and fully incompressible materials, for which the responses to volumetric and deviatoric deformation are significantly different in magnitude, as volume changes are highly or fully constrained.

2.3. Initial and boundary conditions

We complete the problem by specifying the initial and boundary conditions. For the sake of simplicity, we assume zero initial displacements, that is, $\mathbf{u}(\mathbf{X}, 0) = \mathbf{u}_0 \equiv \mathbf{0}$. Hence:

$$\varphi(\mathbf{X}, 0) = \mathbf{X}, \quad \mathbf{F}|_{t=0} \equiv \mathbf{I}, \quad \text{and} \quad J|_{t=0} \equiv 1. \quad (4)$$

We also assume that the initial state of the material is not pre-stressed, so that $\mathbf{u}_0 = \mathbf{0}$ implies a stress-free state. The initial condition for the velocity is given as $\mathbf{v}(\mathbf{X}, 0) = \mathbf{v}_0(\mathbf{X})$ for some function $\mathbf{v}_0 : \mathbb{R}^{n_d} \rightarrow \mathbb{R}^{n_d}$.

The boundary conditions are specified assuming a partition of the boundary $\Gamma = \overline{\Gamma_g} \cup \overline{\Gamma_h}$ such that $\Gamma_g \cap \Gamma_h = \emptyset$. Here Γ_g is the *Dirichlet boundary* on which we enforce the *displacement boundary condition*

$$\mathbf{u}|_{\Gamma_g} = \mathbf{g}(\mathbf{x}, t), \quad (5)$$

and Γ_h is the *Neumann boundary* on which we enforce the *traction boundary condition*

$$\boldsymbol{\sigma} \mathbf{n}|_{\Gamma_h} = \mathbf{t}(\mathbf{x}, t), \quad (6)$$

where \mathbf{n} is the outward-pointing normal on the boundary Γ , and \mathbf{t} is the traction. (We always assume $\Gamma_g = \varphi(\Gamma_g(t=0))$ and $\Gamma_h = \varphi(\Gamma_h(t=0))$.)

3. LINEAR ELASTICITY

The concepts presented in this work can be best understood in the context of linear elasticity. By the infinitesimal strain assumption, we have $\mathbf{x} \approx \mathbf{X}$, $\Omega \approx \Omega_0$, $\nabla_{\mathbf{x}} \approx \nabla_{\mathbf{X}}$ and $\nabla_{\mathbf{X}} \mathbf{u} \ll 1$. Hence $J \approx 1 + \nabla_{\mathbf{X}} \cdot \mathbf{u}$, which implies:

$$\rho_0 \approx (1 + \nabla_{\mathbf{X}} \cdot \mathbf{u}) \rho \approx \rho, \quad (7)$$

and, consequently, the density becomes a datum of the problem rather than a variable. In the remainder of this section, we drop the subscript \mathbf{X} in the spatial derivatives, because no ambiguity will be caused due to the fact that $\nabla_{\mathbf{x}} \approx \nabla_{\mathbf{X}}$.

The stress-strain relationship is given as $\boldsymbol{\sigma} = \mathbf{C}\boldsymbol{\epsilon}$, where $\boldsymbol{\epsilon}(\mathbf{u}) = \nabla^s \mathbf{u}$ is the strain tensor, $\nabla^s = 1/2 (\nabla + \nabla^T)$ is the symmetric part of the gradient, and $\mathbf{C} = [\mathbf{C}_{ijkl}]$ is the fourth-order stiffness tensor, which, for isotropic materials, collapses to

$$\mathbf{C}_{ijkl} = \lambda \delta_{ij} \delta_{kl} + \mu (\delta_{ik} \delta_{jl} + \delta_{il} \delta_{jk}). \quad (8)$$

Here λ and μ are the Lamé coefficients, which are related to the Young's modulus E and the bulk modulus κ by:

$$\lambda = \frac{E\nu}{(1+\nu)(1-2\nu)}, \quad \mu = G = \frac{E}{2(1+\nu)}, \quad \kappa = \lambda + 2\mu/3, \quad (9)$$

where G denotes the shear modulus, and ν is the Poisson ratio. Particularly, for nearly incompressible materials, we are interested in the limit $\nu \rightarrow 0.5^-$. Using the constitutive law (8), we have:

$$p = \kappa \nabla \cdot \mathbf{u}, \quad \text{dev}[\boldsymbol{\sigma}] = 2\mu \text{dev}[\boldsymbol{\epsilon}(\mathbf{u})]. \quad (10)$$

The set of equations that describe the evolution of a mechanical system under small strain and isotropic elastic material behavior are then:

$$\dot{\mathbf{u}} = \mathbf{v} , \quad (11a)$$

$$\rho_0 \dot{\mathbf{v}} = \nabla p + \nabla \cdot (2\mu \mathbf{dev}[\epsilon(\mathbf{u})]) + \rho_0 \mathbf{b} , \quad (11b)$$

$$p = \kappa \nabla \cdot \mathbf{u} , \quad (11c)$$

where all spatial derivatives are computed in the original configuration.

3.1. Connections with the Stokes flow problem

To understand the fundamental issues associated with the numerical approximation of problem (11) using Galerkin finite elements, let us consider the static case and the incompressible limit, for which $\nu \rightarrow 0.5^-$ and $\kappa \rightarrow \infty$. Then the equations (11) reduce to:

$$0 = \nabla p + 2\mu \nabla \cdot \mathbf{dev}[\epsilon(\mathbf{u})] + \rho_0 \mathbf{b} , \quad (12a)$$

$$0 = \nabla \cdot \mathbf{u} , \quad (12b)$$

which are formally identical to the steady Stokes equations for creeping flow if we interpret \mathbf{u} as a velocity instead of a displacement (see also [1]).

Remark 1. The interpretation of \mathbf{u} as velocity for the Stokes flow equations is very important when considering the extension of stabilization techniques to the time-dependent case in nearly or fully incompressible elasticity.

Remark 2. Equations (12) are in *mixed* form, and have been extensively studied in conjunction with the Navier-Stokes equations (see, e.g., the monograph by Brezzi and Fortin [9]).

3.2. General notation

Let us denote by

$$(v, w)_\Omega = \int_\Omega v w \, d\Omega, \quad \text{and} \quad (\mathbf{v}, \mathbf{w})_\Omega = \int_\Omega \mathbf{v} \cdot \mathbf{w} \, d\Omega \quad (13)$$

the $L^2(\Omega)$ - and $(L^2(\Omega))^{n_d}$ -inner products on the interior of the domain Ω and by

$$\langle v, w \rangle_\eta = \int_\eta v w \, d\eta, \quad \eta \subset \Gamma , \quad (14)$$

a functional on a regular subset η of the entire boundary Γ . It will also be important to define quantities that are integrated on the union of the interiors of the elements of the mesh, namely,

$$(v, w)_{\Omega'} = \sum_{e=1}^{n_{el}} \int_{\Omega_e} v w \, d\Omega \quad \text{and} \quad (\mathbf{v}, \mathbf{w})_{\Omega'} = \sum_{e=1}^{n_{el}} \int_{\Omega_e} \mathbf{v} \cdot \mathbf{w} \, d\Omega , \quad (15)$$

where we consider triangulations of the domain Ω into n_{el} elements, with an arbitrary element and its boundary denoted by Ω_e and Γ_e , respectively.

3.3. Review of prior work and its limits of applicability

In the simplest case of piece-wise linear, globally continuous discretization spaces for displacement and pressures - the most relevant to the ongoing discussion - we have:

$$\mathcal{S}_\kappa^h = \mathcal{V}_\kappa^h = \left\{ \psi^h \in (C^0(\Omega))^{n_d} : \psi^h|_{\Omega_e} \in (\mathcal{P}^1(\Omega_e))^{n_d}, \psi^h = \mathbf{0} \text{ on } \Gamma \right\} , \quad (16a)$$

$$\mathcal{S}_\gamma^h = \mathcal{V}_\gamma^h = \left\{ \phi^h \in C^0(\Omega) : \phi^h|_{\Omega_e} \in \mathcal{P}^1(\Omega_e), \phi^h = 0 \text{ on } \Gamma \right\} , \quad (16b)$$

were we have assumed, for the sake of simplicity and without loss of generality, homogeneous Dirichlet boundary conditions for displacement over the entire boundary Γ . We refer to this choice of function spaces as $\mathcal{P}^1/\mathcal{P}^1$. A mixed Galerkin method based on $\mathcal{P}^1/\mathcal{P}^1$ elements is not stable for the incompressible Stokes problem, due to the intuitive fact that there are comparatively too few[†] degrees-of-freedom associated with the discrete displacement space, with respect to the discrete pressure space. In turn, the pressure can be interpreted as a discrete Lagrangian multiplier enforcing the divergence-free constraint [1]. The previous arguments are made precise if the stability of the $\mathcal{P}^1/\mathcal{P}^1$ elements is analyzed using the Ladyzhenskaya-Babuška-Brezzi (LBB) conditions, also known as *inf-sup* conditions [8–10]. The LBB conditions are necessary and sufficient conditions for the existence and uniqueness of the solution to the discrete saddle-point Stokes flow problem. Clearly, a mixed Galerkin formulation with $\mathcal{P}^1/\mathcal{P}^1$ elements does not satisfy the LBB conditions. It is also well known that the standard finite elements that adopt linear displacement and consequently element-wise constant strains/stresses (which we indicate from now on $\mathcal{P}^1/\mathcal{P}^0$) do not perform well in the nearly or fully incompressible case.

3.3.1. A prelude: Introduction to the variational multiscale approach. In recent years Hughes and co-authors developed the theoretical framework for variational multiscale methods [25–27], which have successfully been applied to stabilization of numerical methods for compressible and incompressible flow transport. We present next a very brief and general introduction to the variational multiscale framework in the case of linear operators. An extension of the approach to nonlinear problems is possible, as explained for example in Section 5. Generally speaking, let us consider a linear boundary value problem on a given domain Ω ,

$$\mathcal{L}(\mathbf{Y}) = \mathbf{F}, \quad (17)$$

with appropriate boundary and/or initial conditions (in our case, e.g., $\mathbf{Y} = \{\mathbf{v}, p\}^T$). Introducing a trial solution space \mathcal{S} and a test space \mathcal{V} , compliant with applied boundary conditions, a variational formulation can be formally expressed by seeking $\mathbf{Y} \in \mathcal{S}$ such that for all $\mathbf{W} \in \mathcal{V}$:

$$(\mathbf{W}, \mathcal{L}(\mathbf{Y}))_{\Omega} = (\mathbf{W}, \mathbf{F})_{\Omega}. \quad (18)$$

Here, for the sake of simplicity and without loss of generality, we have omitted boundary integrals, which may be present in the more general case. The variational multiscale approach starts with a decomposition of the function spaces as

$$\mathcal{S} = \mathcal{S}^h \oplus \mathcal{S}', \quad (19)$$

$$\mathcal{V} = \mathcal{V}^h \oplus \mathcal{V}', \quad (20)$$

where \mathcal{S}^h is the discrete spaces used to represent the numerical solution (with associated test space \mathcal{V}^h), while \mathcal{S}' and \mathcal{V}' are infinite dimensional complement spaces. Fundamentally, $\mathbf{Y}' \in \mathcal{S}'$, represents the error between the numerical and exact solutions of the problem. Accordingly \mathcal{V}' represents the test space corresponding to the fine-scale trial space \mathcal{S}' . Consider now equation (18) tested on the space \mathcal{S}^h , namely:

$$(\mathbf{W}^h, \mathcal{L}(\mathbf{Y}^h))_{\Omega} + (\mathcal{L}^* \mathbf{W}^h, \mathbf{Y}')_{\Omega} = (\mathbf{W}^h, \mathbf{F})_{\Omega}, \quad (21)$$

where \mathcal{L}^* is the formal adjoint of the operator \mathcal{L} (here we are slightly abusing notation, since \mathcal{L}^* may include boundary terms). Equation (21) is also termed the coarse-scale problem. Analogously, we can define a fine-scale problem

$$(\mathbf{W}', \mathcal{L}(\mathbf{Y}'))_{\Omega} = -(\mathbf{W}', \mathcal{L}(\mathbf{Y}^h) - \mathbf{F})_{\Omega}, \quad (22)$$

which is inherently infinite dimensional. As such, its exact solution would involve the same effort as finding the exact solution of the original problem (17). However, if the goal of the variational

[†]similar to the case of $\mathcal{P}^1/\mathcal{P}^0$ elements, prone to volumetric locking.

multiscale approach is to improve the stability properties of the original method, it is possible to find suitable approximations to the exact solution of (22). A common choice is the pointwise *ansatz*:

$$\mathbf{Y}' = -\boldsymbol{\tau}(\mathcal{L}(\mathbf{Y}^h) - \mathbf{F}), \quad (23)$$

where the matrix $\boldsymbol{\tau}$ can be interpreted as an approximation to the element average of fine-scale Green's function solving (22). Substituting (23) into the coarse-scale equations (21), a modified discretization is obtained, namely:

$$(\mathbf{W}^h - \boldsymbol{\tau}^T \mathcal{L}^* \mathbf{W}^h, \mathcal{L}(\mathbf{Y}^h))_{\Omega} = (\mathbf{W}^h - \boldsymbol{\tau}^T \mathcal{L}^* \mathbf{W}^h, \mathbf{F})_{\Omega}, \quad (24)$$

which clearly has the structure of a Petrov-Galerkin method, since the equation are now tested on the shape function vector $\mathbf{W}^h - \boldsymbol{\tau}^T \mathcal{L}^* \mathbf{W}^h$. The modified formulation (24) typically enjoys improved stability without precluding accuracy, as residual consistency is maintained.

Remark 3. For the sake of clarity and brevity in the presentation of the key ideas, we have omitted the case - very relevant for piecewise linear interpolations - in which certain terms in the base variational form are integrated by parts. The variational multiscale approach can of course accommodate this situation, as shown in [27].

3.3.2. Seminal contributions to stabilized methods for the Stokes flow. In the work of Hughes, Franca, and Balestra [12], an equal-order approximation to the Stokes problem is considered. The key idea there was to “rebalance” the pressure/displacement degrees-of-freedom by adding a discrete enrichment to the displacement field, and circumventing the LBB stability condition requirements on discrete approximation spaces. The work in [12] contained a proof of stability and convergence and was instrumental in the development of robust stabilized formulations for the Navier-Stokes equations. In [13, 15] an extension to static problems in linear elasticity was also considered, and several other contributions followed with applications to linear and nonlinear solid mechanics [16–24, 38–43, 67–71, 73, 74].

In what follows, we provide a more modern presentation of the stabilized formulation in [12], by means of the variational multiscale approach. The stabilized variational statement of the Stokes problem reads:

Find $p^h \in \mathcal{S}_{\gamma}^h$, $\mathbf{u}^h \in \mathcal{S}_{\kappa}^h$, such that, $\forall \phi^h \in \mathcal{V}_{\gamma}^h$, $\forall \boldsymbol{\psi}^h \in \mathcal{V}_{\kappa}^h$:

$$0 = (\nabla \cdot \boldsymbol{\psi}^h, p^h)_{\Omega} + (\nabla \boldsymbol{\psi}^h, 2\mu \operatorname{dev}[\boldsymbol{\epsilon}(\mathbf{u}^h)])_{\Omega} - (\boldsymbol{\psi}^h, \rho_0 \mathbf{b})_{\Omega}, \quad (25a)$$

$$0 = (\phi^h, \nabla \cdot \mathbf{u}^h)_{\Omega} - (\nabla \phi^h, \mathbf{u}')_{\Omega'}, \quad (25b)$$

where the term \mathbf{u}' in equation (25b) represents an *enrichment* of the displacement solution to prevent oscillations in the discrete pressure field. In [12] the following expression for \mathbf{u}' was proposed, in terms of the momentum balance residual:

$$\mathbf{u}' = \boldsymbol{\tau} (\nabla p^h + \nabla \cdot (2\mu \operatorname{dev}[\boldsymbol{\epsilon}(\mathbf{u}^h)]) + \rho_0 \mathbf{b}), \quad (26a)$$

$$\boldsymbol{\tau} = c_{\tau} \frac{h^2}{2\mu}. \quad (26b)$$

Here h is the characteristic element length and c_{τ} is a constant. An appropriate value for c_{τ} can be estimated using inverse inequalities [12], which yield a typical range $c_{\tau} \in [0.1, 1]$. In a recent paper, Nakshatrala, Masud, and Hjelmstad [22] proposed a way to estimate c_{τ} by means of localized element bubble functions.

Remark 4. The term $\boldsymbol{\tau}$ in (26a) represents an approximation to the average of the element's fine-scale Green's function [25].

For piecewise linear functions, the divergence of the coarse-scale deviatoric strain vanishes, so that (28) reduces to:

$$0 = (\boldsymbol{\psi}^h, \rho_0 \mathbf{b})_{\Omega} + (\nabla \cdot \boldsymbol{\psi}^h, p^h)_{\Omega} + (\nabla \boldsymbol{\psi}^h, 2\mu \operatorname{dev}[\boldsymbol{\epsilon}(\mathbf{u}^h)])_{\Omega}, \quad (27a)$$

$$0 = (\phi^h, \nabla \cdot \mathbf{u}^h)_{\Omega} - (\nabla \phi^h, \boldsymbol{\tau}(\nabla p^h + \rho_0 \mathbf{b}))_{\Omega'}. \quad (27b)$$

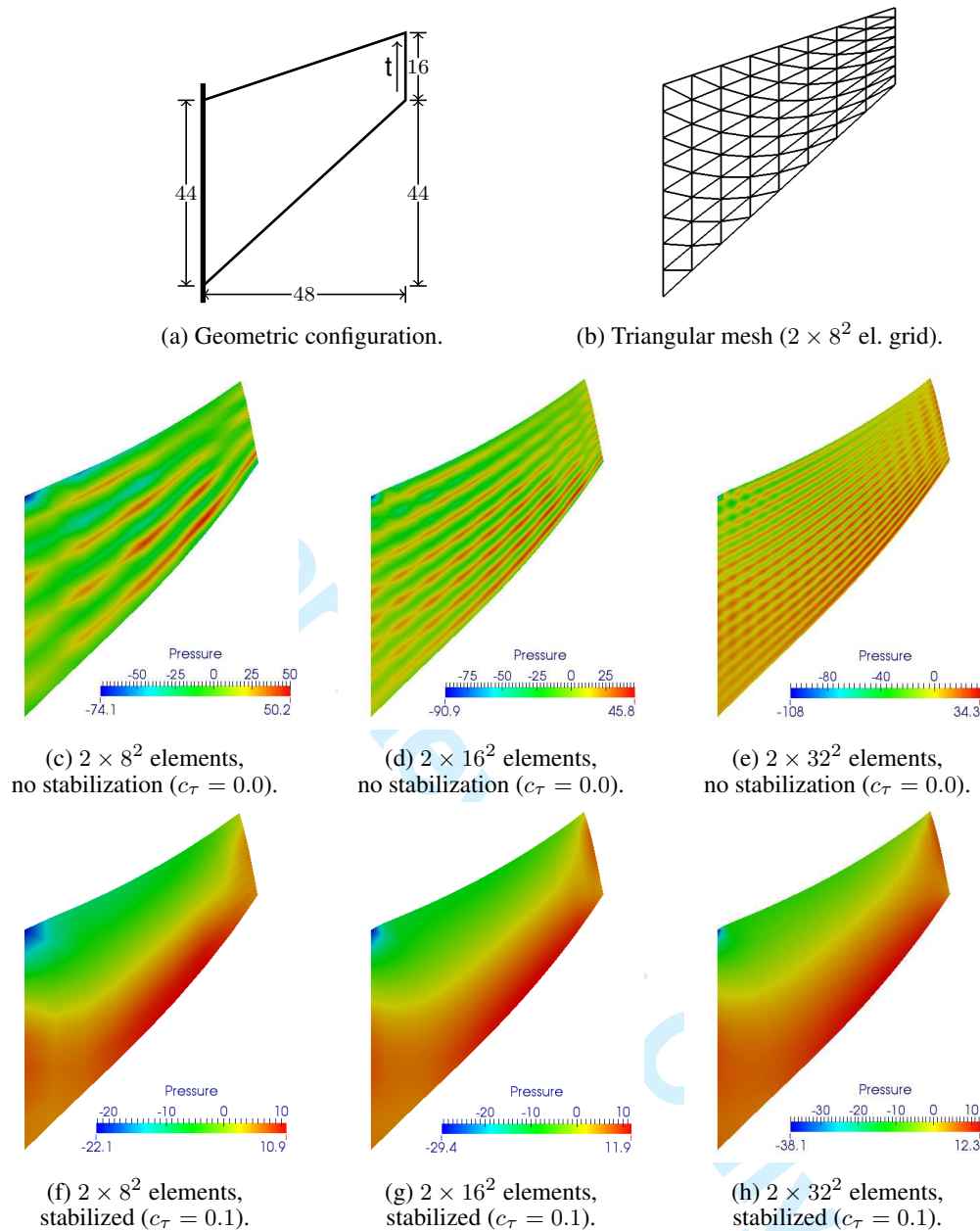


Figure 1. The Cook's membrane test for static incompressible linear elasticity, using the method of Hughes, Franca, and Balestra [12].

As already mentioned, [12] contained a proof of consistency, stability, and convergence of this method for any interpolation order. In the case of piecewise linear finite elements, it is shown that the displacement is second-order accurate, while the order of convergence for the pressure is 1.5. Both convergence rates are in terms of L^2 -norms. The presented stabilized method has been extended to linear incompressible isotropic elasticity in [15] and also problems in finite elasto-visco-plasticity in [16–20, 67–71].

Remark 5. The reduced order of convergence for the pressure is considered a suboptimal feature in the context of the Stokes or Navier-Stokes equations, but for solid dynamics computations, in which the approximation of the deviatoric component of the stress is only first-order accurate, this aspect does not pose any particular problem to the overall accuracy of the stress approximation.

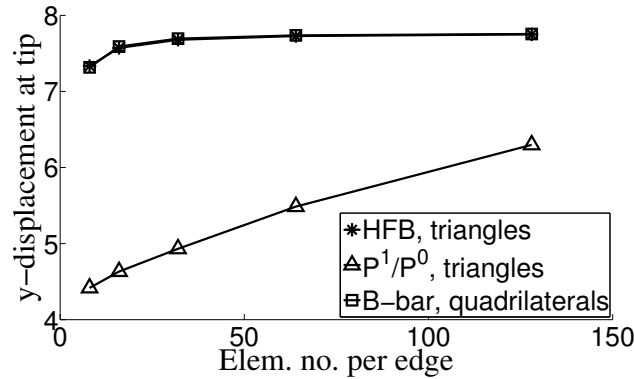


Figure 2. The Cook's membrane test for static incompressible linear elasticity: Convergence of the tip displacement as a function of the number of elements. Comparison among the HFB method [12] (with $c_\tau = 0.1$), the standard P^1/P^0 element, and the Q^1 B-bar element. Observe that the HFB and Q^1 B-bar solutions are overlapped, while the P^1/P^0 solution shows slow convergence, typical of locking.

Remark 6. The idea behind the stabilized approach is to estimate the numerical error in displacement, represented by \mathbf{u}' , using the residual of the governing equations (the momentum equations to be more specific) and then feed back this information into the discrete equations. This first stage of the process (the fine-scale estimation using residual information) is consistent with *a posteriori* error estimation techniques [93–95].

3.3.3. Testing the approach in [12]: Static Cook's membrane test. A standard problem in which P^1/P^1 elements lead to oscillatory pressures is the Cook's membrane problem [96]. The geometric setup of the problem is shown in Figure 1a, and a typical triangular mesh obtained by splitting every element of an underlying quadrilateral grid into two triangles is shown in Figure 1b.

The material is modeled as linearly elastic with normalized density $\rho = 1.0$, Young's Modulus $E = 250.0$, and Poisson's ratio $\nu = 0.49995$. As shown in Figure 1a, zero displacement Dirichlet boundary conditions are imposed at the left vertical edge of the membrane, while a uniform vertical shear traction t is imposed on the vertical right edge, so that the net vertical force is $V = 6.25$. The two horizontal edge are traction free.

Because the problem is nearly incompressible, and not fully incompressible, we consider a fairly standard extension of the HFB as follows:

$$0 = (\nabla \cdot \psi^h, p^h)_\Omega + (\nabla \psi^h, 2\mu \operatorname{dev}[\epsilon(\mathbf{u}^h)])_\Omega - (\psi^h, \rho_0 \mathbf{b})_\Omega, \quad (28a)$$

$$(\phi^h, \frac{1}{\kappa} p^h)_\Omega = (\phi^h, \nabla \cdot \mathbf{u}^h)_\Omega - (\nabla \phi^h, \mathbf{u}')_{\Omega'}. \quad (28b)$$

As shown in Figures 1c–1e, the mixed Galerkin P^1/P^1 solution develops unstable pressure modes when no stabilization is applied. These modes have been widely documented in the literature [10]. On the other hand, the HFB method converges as shown in Figures 1f–1h, without any oscillations. Note also in Figure 2 that the tip displacement shows relatively rapid convergence on relatively coarse grids, and indication that volumetric locking is *not* occurring. In the same picture, we compare the stabilized method with a Q^1 finite element on hexahedral elements with reduced selective integration (see [1], p. 218), formally equivalent to a B-bar method (see [1], p. 232) in Cartesian coordinates (we denote this method by Q^1 B-bar). The B-bar method is the state of the practice in modern commercial software, and is praised as a very good compromise between computational cost and overall performance. Note that the HFB and B-bar solutions are virtually overlapped in Figure 2.

3.3.4. Limitations of the approach [12] in transient dynamics. When considering the time-dependent case, it is important to realize that there is a fundamental departure between the structure

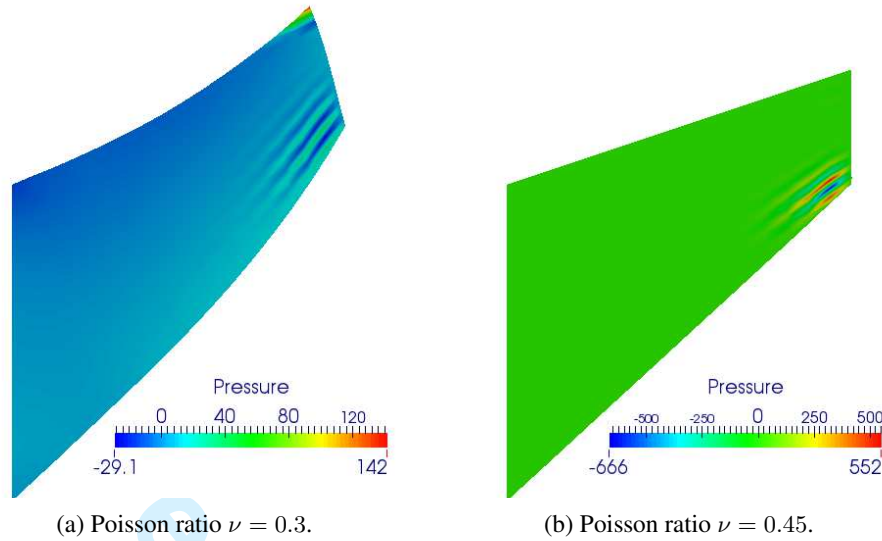


Figure 3. The dynamic Cook's membrane test for various levels of compressibility, using the method of Hughes, Franca, and Balestra [12]. All computations are performed on a grid of 2×16^2 elements, with $\alpha_{\text{eff}} = 0.9$, and $c_\tau = 0.1$. It was not possible to run computations in the true incompressible limit, as catastrophic instabilities developed. Here we report the results for Poisson ratios 0.3 and 0.45, at time $T = 7.415$ and 0.063 respectively (at these time instants the computations are about to abort). We also note that similar results are obtained reducing the α_{eff} to 0.1.

of the unsteady Stokes flow and the transient elasticity equations, as already alluded to in Remark 1 of Section 3.1. Fundamentally, in the Stokes flow equations, \mathbf{u} represents a velocity and not a displacement, and consequently, only one time derivative is needed to obtain the inertia terms. Instead, in the case of the elasticity equations, two time derivatives are applied to \mathbf{u} in order to obtain the inertia term $\rho_0 \ddot{\mathbf{u}} = \rho_0 \dot{\mathbf{v}}$, and the equations acquire the structure of the d'Alembert operator, characterizing waves in continuous media.

As a result, while the unsteady Stokes flow equations are *parabolic* in nature, the transient elasticity equations are *hyperbolic*. In the incompressible limit, the equations of elasticity become *degenerate hyperbolic*, as the pressure assumes the role of the Lagrange multiplier needed to impose the divergence-free constraint on the displacement (or velocity) field: Bulk (volumetric) waves are prevented, but shear (deviatoric) waves can still propagate.

Remark 7. If we consider the theory of stabilization by means of variational multiscale methods [27], there are fundamental differences in the strategies adopted to stabilized elliptic/parabolic equations, and hyperbolic systems [55–65]. Although no mention of this fact is found in the literature of stabilized method for elasticity problems, it is very natural to expect that many of the stabilization strategies for the static case would not generalize easily to the transient dynamics case.

Our doubts are confirmed when we attempt to use the stabilization proposed in [12] for time dependent problems in nearly or fully incompressible linear elasticity. Specifically, we considered the following straightforward extension of the method in [12] to the time dependent case:

$$(\psi^h, \dot{\mathbf{u}})_\Omega = (\psi^h, \mathbf{v})_\Omega, \quad (29a)$$

$$0 = (\psi^h, \rho_0 \dot{\mathbf{v}})_\Omega + (\nabla \cdot \psi^h, p^h)_\Omega + (\nabla \psi^h, 2\mu \mathbf{dev}[\epsilon(\mathbf{u}^h)])_\Omega - (\psi^h, \rho_0 \mathbf{b})_\Omega, \quad (29b)$$

$$(\phi^h, p^h)_\Omega = (\phi^h, \kappa \nabla \cdot \mathbf{u}^h)_\Omega + (\nabla \phi^h, \kappa \tau(\rho_0 \dot{\mathbf{v}} - \nabla p^h - \nabla \cdot (2\mu \mathbf{dev}[\epsilon(\mathbf{u}^h)] - \rho_0 \mathbf{b}))_\Omega. \quad (29c)$$

In the case of fully incompressible behavior, (29c) simplifies to

$$0 = (\phi^h, \nabla \cdot \mathbf{u}^h)_\Omega + (\nabla \phi^h, \tau(\rho_0 \dot{\mathbf{v}} - \nabla p^h - \nabla \cdot (2\mu \mathbf{dev}[\epsilon(\mathbf{u}^h)] - \rho_0 \mathbf{b}))_\Omega. \quad (30)$$

We applied this stabilized approach to a *dynamic* version of the Cook's membrane test, in which boundary conditions and loads are the same as the ones used in the static case, with homogeneous initial conditions on the velocity and displacement fields. The expected solution will oscillate about the static equilibrium state computed in Section 3.3.3.

Remark 8. We note that (29a) indicates a nodal update of the displacement field using the numerical solutions of the velocity fields. This nodal procedure is equivalent to solve the variational problem using consistent mass matrix on both sides, (in particular, no mass-lumping on the left hand side).

The results of the dynamic Cook's membrane computations in Figure 3 may seem surprising at first, but indeed they are confirming the interpretations outlined above: It was not possible to successfully run the computations in the incompressible limit, as the simulations would fail almost immediately after launch. We managed however to run for a few time steps with Poisson's ratios $\nu = 0.3$ and $\nu = 0.45$, for which very large oscillations rapidly pollute the computed solution.

3.4. A new variational multiscale approach using pressure rate updates.

With the purpose of designing an alternative stabilized formulation in the transient case, we take now a *detour* and consider the equations of Lagrangian compressible shock hydrodynamics [92, 97–99] - a purely hyperbolic system. It may seem odd, at first sight, that we consider the case of a highly compressible fluid to get some inspiration for a nearly or fully incompressible solid problem, but we ask the reader to be patient, as this step will appear more clear momentarily, when analogies between the two systems will be considered. The key idea here is that since solid dynamics is governed by a hyperbolic system of equations, we take inspiration from previous work with fluids in this context.

3.4.1. The rate form of the pressure constitutive model. As shown in [92], the energy equation for a compressible inviscid fluid in Lagrangian coordinates can be written in terms of a pressure update equation, namely:

$$0 = \rho \dot{e} + p \nabla_{\mathbf{x}} \cdot \mathbf{v} = \rho \left. \frac{\partial e}{\partial p} \right|_{\rho} (\dot{p} + \rho c_s^2 \nabla_{\mathbf{x}} \cdot \mathbf{v}) = \rho \left. \frac{\partial e}{\partial p} \right|_{\rho} (\dot{p} + \kappa_f \nabla_{\mathbf{x}} \cdot \mathbf{v}) , \quad (31)$$

where e is the internal energy, c_s is the speed of sound, $\kappa_f = \rho c_s^2$ is the fluid's bulk modulus, and p is the pressure of the fluid (the sign of the fluid mechanics convention is opposite with respect to the solid mechanics convention). The identity (31) is obtained by means of the Gibbs thermodynamics identity, and some standard calculus derivations (see [99] for more details). Observing that the term $\rho \left. \frac{\partial e}{\partial p} \right|_{\rho}$ is typically different from zero unless phase changes occur, the energy equation can be simplified to

$$0 = \dot{p} + \kappa_f \nabla_{\mathbf{x}} \cdot \mathbf{v} . \quad (32)$$

Equation (32) formally applies to the nonlinear case, but can be further simplified in the linearized limit of the Lagrangian shock hydrodynamics equations, namely, the equations of non-dissipative acoustics. In this case, $\rho \approx \rho_0$, c_s , and κ_f are constant, and it is not very difficult to realize that (32) also represents the rate form of equation (11c), where a time derivative is applied on both the right- and left-hand side of this equation.

3.4.2. A variational multiscale approach in rate form. Replacing κ_f with κ , a general weak formulation of (11a), (11b), and (32) can be obtained. Namely:

Solve for $\mathbf{u}^h, \mathbf{v}^h \in \mathcal{S}_{\kappa}^h$ and $p^h \in \mathcal{S}_{\gamma}^h$, such that, for all $\boldsymbol{\psi}^h \in \mathcal{V}_{\kappa}^h$ and $\phi^h \in \mathcal{V}_{\gamma}^h$:

$$0 = (\boldsymbol{\psi}^h, \dot{\mathbf{u}}^h - \mathbf{v}^h)_{\Omega} , \quad (33a)$$

$$0 = (\boldsymbol{\psi}^h, \rho_0 \dot{\mathbf{v}}^h)_{\Omega} + (\nabla \cdot \boldsymbol{\psi}^h, p^h)_{\Omega} + (\nabla^s \boldsymbol{\psi}^h, 2\mu \operatorname{dev}[\boldsymbol{\epsilon}(\mathbf{u}^h)])_{\Omega} - (\boldsymbol{\psi}^h, \rho_0 \mathbf{b})_{\Omega} , \quad (33b)$$

$$0 = (\phi^h, \kappa^{-1} \dot{p}^h - \nabla \cdot \mathbf{v}^h)_{\Omega} + (\nabla \phi^h, \mathbf{v}^h)_{\Omega} , \quad (33c)$$

where

$$\mathbf{v}' = -\frac{\tau}{\rho_0} (\rho_0 \dot{\mathbf{v}}^h - \nabla p^h - \nabla \cdot (2\mu \mathbf{dev}[\boldsymbol{\epsilon}(\mathbf{u}^h)]) - \rho_0 \mathbf{b}), \quad (34)$$

i.e., \mathbf{v}' is proportional to the residual of the resolved solutions through a scaling parameter τ , which is a characteristic time scale. Specific definitions for τ will be analyzed in Section 3.4.5.

This new approach proved stable, robust and accurate in numerical tests that are detailed in Section 4, including the dynamic version of the Cook's membrane test in the nearly incompressible limit. In what follows, we will indicate this method as *dynamic variational multiscale approach* or, in short, *D-VMS*.

3.4.3. Interpretation of the proposed stabilization strategy: Accumulation in time of the fine-scales.

It may seem at this point quite strange that the simple modification applied, namely using the rate form of the pressure constitutive equation, could be so important. However, consider the integral in time of the stabilized equation for the pressure in semi-discretized form, in which the discretization is applied only in space, and the time is still a continuum:

$$0 = (\phi^h, \kappa^{-1} p^h(t))_{\Omega} - (\phi^h, \kappa^{-1} p^h(0))_{\Omega} - \int_0^t (\phi^h, \nabla \cdot \mathbf{v}^h)_{\Omega} dt + \int_0^t (\nabla \phi^h, \mathbf{v}')_{\Omega} dt. \quad (35)$$

The last term in the equation, the integral of the fine-scale velocity, can also be interpreted as the *cumulative* fine-scale displacement, that is $\mathbf{u}'(t) = \int_0^t \mathbf{v}'(\tilde{t}) d\tilde{t}$. Assuming that at $t = 0$ displacements and pressures are zero (i.e. the solid is not pre-stressed at the initial time of the simulation), and using $\mathbf{u}^h(t) = \int_0^t \mathbf{v}^h(\tilde{t}) d\tilde{t}$, we can further simplify (35) to:

$$(\phi^h, \kappa^{-1} p^h(t))_{\Omega} = (\phi^h, \nabla \cdot \mathbf{u}^h(t))_{\Omega} - (\nabla \phi^h, \mathbf{u}')_{\Omega}, \quad (36)$$

which is formally identical to (29c), but has one crucial difference, in that the fine-scale displacement is now given by

$$\mathbf{u}'(t) = -\frac{\tau}{\rho_0} \int_0^t (\rho_0 \dot{\mathbf{v}}^h - \nabla p^h - \nabla \cdot (2\mu \mathbf{dev}[\boldsymbol{\epsilon}(\mathbf{u}^h)]) - \rho_0 \mathbf{b}) dt, \quad (37)$$

as opposed to

$$\mathbf{u}'(t) = -\frac{\tau}{\rho_0} (\rho_0 \dot{\mathbf{v}}^h - \nabla p^h - \nabla \cdot (2\mu \mathbf{dev}[\boldsymbol{\epsilon}(\mathbf{u}^h)]) - \rho_0 \mathbf{b}). \quad (38)$$

This analysis indicates that in the case of transient solid mechanics computations, the momentum balance residual can be successfully used as a very good estimate for the fine-scale velocity, but not for the fine-scale displacement. The estimate of the fine-scale displacement field requires instead the accumulation of the fine-scale velocity contributions over time.

Remark 9. Of course, comparing (37) and (38), the parameter τ have different units, but this should not be a surprise, since the residual of the momentum balance is used in (37) to estimate \mathbf{v}' and in (38) to estimate \mathbf{u}' .

Remark 10. In the case of linear finite element spaces, the divergence of the stress deviator $\nabla \cdot (2\mu \mathbf{dev}[\boldsymbol{\epsilon}(\mathbf{u}^h)])$ in (34) vanishes, and the residual is incomplete. One important note is that although this fact might produce excessive numerical dissipation in the compressible regime, this was not observed to be the case in nearly and fully incompressible elastic regimes. Fundamentally, when volume changes are constrained, the shear component of the stress becomes negligible with respect to the hydrostatic component of the stress, which acts a Lagrange multiplier. This was our experience in all computations performed. There are a few options to incorporate the effect of the term $\nabla \cdot (2\mu \mathbf{dev}[\boldsymbol{\epsilon}(\mathbf{u}^h)])$ in the computations: One is a reconstruction via L_2 - projection (as suggested in [100] for the Navier-Stokes equations); alternatively, an explicit representation can be attempted using inter-element boundary integrals (Dirac distribution layers). This ideas are currently under evaluation and testing, and we hope to report soon about the outcomes of these investigations.

3.4.4. Choice of the parameter τ . The parameter τ in (34) is an intrinsic time-scale and can be estimated in various ways. From the point of view of the variational multi-scale analysis [27], it also represents the integral effect of the Green's function associated with the fine-scale problem. A simple choice for τ is to take $\tau \propto \Delta t$, and more specifically

$$\tau = \frac{c_\tau}{\alpha_{\text{cfl}}} \Delta t. \quad (39)$$

In our definition, we divide the time step Δt by the global Courant-Friedrichs-Lewy (CFL) number α_{cfl} , so that τ is scaled with the time step corresponding to a unit Courant-Friedrichs-Lewy number. This choice was adopted already in [92], in order to prevent the stabilizing term to vanish in the limit of small time steps. An alternative definition, which also does not suffer from the small time step problem is

$$\tau = c_\tau \frac{h^e}{c_{\max}}, \quad (40)$$

where h^e is a reference element length (computed as the largest length of edges of the element) and c_{\max} is a wave speed. In the case of nearly incompressible materials, bulk waves are still present and one could take the speed $c_{\max} = \sqrt{(\kappa + 3\mu/4)/\rho_0}$ of plane waves. If instead the fully incompressible case were to be considered, bulk waves do not propagate through the material, leading to the choice $c_{\max} = \sqrt{\mu/\rho_0}$.

Remark 11. Clearly, (39) provides a uniform distribution of the stabilization parameter over the solid domain, whereas (40) leads to a localized distribution.

3.4.5. Algorithmic implementation. We describe next an implementation of the proposed method in the context of explicit time integration. The time integrator is of mid-point type, combined with a fixed-point predictor/multi-corrector strategy [92, 101]. The implicit version of the proposed algorithm is straightforward and is the object of ongoing research. We also note that the first two iterations of the method correspond to the RK2-TVD scheme (Runge-Kutta total variation diminishing method of order two). In what follows, we use the subscript n and $n+1$ to denote the solution at time step t_n and $t_{n+1} = t_n + \Delta t_n$, respectively. The \mathcal{P}^1 approximation to the solutions fields reads:

$$\mathbf{u}^h = \sum_{A=1}^{n_{np}} N_A \mathbf{u}_A, \quad \mathbf{v}^h = \sum_{A=1}^{n_{np}} N_A \mathbf{v}_A, \quad \text{and} \quad p^h = \sum_{A=1}^{n_{np}} N_A p_A, \quad (41)$$

where N_A is the shape function associated with node A in the global finite element numbering (with n_{np} the total number of nodes of the grid), and \mathbf{u}_A , \mathbf{v}_A , and p_A are the corresponding values for the arrays of displacement \mathbf{u} , velocity \mathbf{v} , and pressure p degrees of freedom, respectively. We summarize next the update algorithm from the state $\{\mathbf{u}_n, \mathbf{v}_n, p_n\}$ to the state $\{\mathbf{u}_{n+1}, \mathbf{v}_{n+1}, p_{n+1}\}$.

For this purpose, we denote by the superscript (i) the i^{th} -iterate of the solution (at a certain time step). We also use $\mathbf{u}_{n+1/2}^{(i)} = (\mathbf{u}_n + \mathbf{u}_{n+1}^{(i)})/2$ to denote the average of quantity \mathbf{u} between time steps. Mass matrices for the momentum and pressure equations will be denoted by

$$\mathbf{M}_v = [\text{diag}(\mathbf{M}_0, \mathbf{M}_0, \mathbf{M}_0)], \quad \mathbf{M}_0 = \mathbf{L}([\mathbf{M}_{0;A}]), \quad \mathbf{M}_{0;A} = (N_A, \rho_0), \quad (42)$$

and

$$\mathbf{V}_0 = \mathbf{L}([\mathbf{V}_{0;A}]), \quad \mathbf{V}_{0;A} = (N_A, 1), \quad (43)$$

respectively, where \mathbf{L} denotes the standard row-sum lumping algebraic operator. Note that \mathbf{V}_0 is in fact the array of nodal volumes.

Next we define the lumped mass matrix $\mathbf{M}_v = [\text{diag}(\mathbf{M}_0, \mathbf{M}_0, \mathbf{M}_0)]$ and the lumped volume matrix $\mathbf{M}_s = [\text{diag}(\mathbf{V}_0)]$, respectively. Then the variational forms (33c), (33b), and (33a) yield, respectively:

Algorithm 1 Predictor/multi-corrector update of $\{\mathbf{u}_{n+1}, \mathbf{v}_{n+1}, \mathbf{p}_{n+1}\}$ from $\{\mathbf{u}_n, \mathbf{v}_n, \mathbf{p}_n\}$.

- 1: Retrieve the loop parameter i_{\max} .
 - 2: Set $\{\mathbf{u}_{n+1}^{(0)}, \mathbf{v}_{n+1}^{(0)}, \mathbf{p}_{n+1}^{(0)}\} = \{\mathbf{u}_n, \mathbf{v}_n, \mathbf{p}_n\}$.
 - 3: **for** $i = 0, \dots, i_{\max} - 1$ **do**
 - 4: Compute τ using (39) or (40).
 - 5: Assemble $\mathbf{W}_{n+1/2}^{(i)}$.
 - 6: Pressure update: $\mathbf{p}_{n+1}^{(i+1)} = \mathbf{p}_n - \Delta t_n [\mathbf{V}_s]^{-1} \mathbf{W}_{n+1/2}^{(i)}$.
 - 7: Assemble $\mathbf{F}_{n+1/2}^{(i,i+1)}$.
 - 8: Velocity update: $\mathbf{v}_{n+1}^{(i+1)} = \mathbf{v}_n - \Delta t_n [\mathbf{M}_v]^{-1} \mathbf{F}_{n+1/2}^{(i,i+1)}$.
 - 9: Displacement update: $\mathbf{u}_{n+1}^{(i+1)} = \mathbf{u}_n + \Delta t_n \mathbf{v}_{n+1}^{(i+1)}$.
 - 10: **end for**
 - 11: Set $(\mathbf{u}_{n+1}, \mathbf{v}_{n+1}, \mathbf{p}_{n+1}) = (\mathbf{u}_{n+1}^{(i_{\max})}, \mathbf{v}_{n+1}^{(i_{\max})}, \mathbf{p}_{n+1}^{(i_{\max})})$.
-

$$\mathbf{V}_s \frac{\mathbf{p}_{n+1}^{(i+1)} - \mathbf{p}_n}{\Delta t_n} = -\mathbf{W}_{n+1/2}^{(i)}, \quad (44a)$$

$$\mathbf{M}_v \frac{\mathbf{v}_{n+1}^{(i+1)} - \mathbf{v}_n}{\Delta t_n} = -\mathbf{F}_{n+1/2}^{(i,i+1)}, \quad (44b)$$

$$\frac{\mathbf{u}_{n+1}^{(i+1)} - \mathbf{u}_n}{\Delta t_n} = \mathbf{v}_{n+1/2}^{(i+1)}, \quad (44c)$$

where $i = 0, 1, \dots, i_{\max} - 1$. The array $\mathbf{W}_{n+1/2}^{(i)}$ is computed according to (33b) as:

$$\mathbf{W}_{n+1/2}^{(i)} = (N_A, \kappa \nabla \cdot \mathbf{v}_{n+1/2}^{(i)})_{\Omega} - (\nabla N_A, \kappa \mathbf{v}')_{\Omega}, \quad (45)$$

using

$$\mathbf{v}' = -\frac{\tau}{\rho_0} \left(\rho_0 \frac{\mathbf{v}_{n+1}^{(i)} - \mathbf{v}_n}{\Delta t_n} - \nabla p_{n+1/2}^{(i)} - \rho_0 \mathbf{b}_{n+1/2} \right). \quad (46)$$

Similarly, $\mathbf{F}_{n+1/2}^{(i,i+1)}$ is computed according to (33c) as:

$$\mathbf{F}_{n+1/2}^{(i,i+1)} = -(\partial_j (N_A \mathbf{e}_j), p_{n+1/2}^{(i+1)})_{\Omega} - (\nabla^s (N_A \mathbf{e}_j), 2\mu \mathbf{dev}[\epsilon(\mathbf{u}_{n+1/2}^{(i)})])_{\Omega} + (N_A \mathbf{e}_j, \rho_0 \mathbf{b})_{\Omega}. \quad (47)$$

When choosing how many iterations i_{\max} to perform, the main considerations are accuracy in time and the angular momentum/invariance preservation [101]. In particular, the predictor/multi-corrector method under consideration is second-order accurate in time for all $i_{\max} \geq 2$, and converges to a mid-point time-integrator as $i_{\max} \rightarrow \infty$. The mid-point time integrator is known to preserve discrete angular momentum exactly, and previous work [101] suggested that, typically, for $i_{\max} \geq 3$, the angular momentum conservation error is negligible for any practical purposes. Thus, in all the computations in this paper, we choose $i_{\max} = 3$. The entire algorithm is summarized as Algorithm 1. The time-step size Δt_n is selected so that it satisfies the Courant-Frederich-Levy condition:

$$\Delta t = \alpha_{\text{cfl}} \min_{\Omega_e \in \Omega_0} \frac{h^e}{\sqrt{(\kappa + 3\mu/4)/\rho_0}}, \quad (48)$$

where $\alpha_{\text{cfl}} = 0.9$ is our preferred choice, h^e is the reference length associated with an element Ω_e (the diameter of the element's inscribed circle or sphere, in our case), and the minimum is taken over all elements in the initial configuration. In the case of linear problems, Δt is only computed once and used for all subsequent time steps: For this reason, its computation is not included in Algorithm 1.

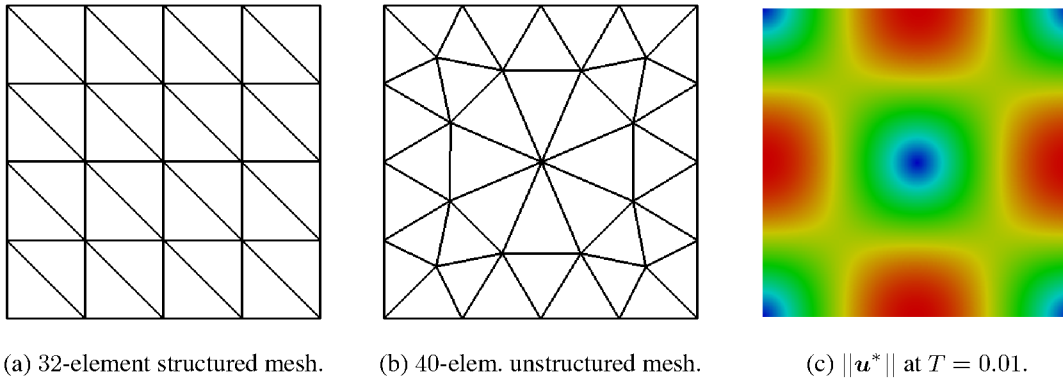


Figure 4. Two-dimensional swinging plate problem: Examples of structured and unstructured meshes, and norm of the displacement reference solution $\|\mathbf{u}^*\|$ at $T = 0.01$.

4. NUMERICAL RESULTS: LINEAR ELASTICITY

A number of numerical examples is presented next to test the stability and accuracy of the proposed D-VMS approach in the case of linear problems. The stabilization term τ is computed using (39) with $\alpha_{\text{eff}} = 0.9$. The value of c_τ is optimized according to the number of space dimensions: For two-dimensional problems, under plain strain assumption, we choose to set $c_\tau = 0.5$, while for three-dimensional computations, we set $c_\tau = 0.15$. There is however some freedom in the choice of the stabilization constant, and values larger by 100% would still yield acceptable results. Our strategy in optimizing c_τ is to select the value that provides stable, non-oscillatory computations with the minimum amount of numerical dissipation. In what follows, we denote by HFB the stabilization of [12] extended as in equation (26) to the time dependent case, with $c_\tau = 0.1$ (value also recommended in [12]).

4.1. Two-dimensional swinging plate test I: Comparison of HFB and D-VMS approaches

The swinging plate test [46, 47] is a valuable test in evaluating the order of convergence of the proposed method. The domain is the square $\Omega = [0, 2\text{ m}]^2$, and the analytical solution for the displacement \mathbf{u}^* is given by:

$$\mathbf{u}^*(\mathbf{x}, t) = U_0 \sin(\omega t) \begin{bmatrix} -\sin\left(\frac{\pi}{2}x\right) \cos\left(\frac{\pi}{2}y\right) \\ \cos\left(\frac{\pi}{2}x\right) \sin\left(\frac{\pi}{2}y\right) \end{bmatrix}, \quad (49)$$

where $U_0 = 10^{-2}$ m is a constant. We consider the material property $E = 1.7 \times 10^6$ Pa and $\rho_0 = 1.1 \times 10^3$ kg/m³. Note that (49) leads to a divergence-free displacement/velocity fields, thus the exact pressure is $p^* = 0$. In addition, by defining the angular frequency ω as:

$$\omega = \frac{\pi}{2} \sqrt{\frac{2\mu}{\rho_0}}, \quad (50)$$

the variables \mathbf{u}^* , $\mathbf{v}^* = \dot{\mathbf{u}}^*$, and $p^* = 0$ solve (11) with no body force (i.e., $\mathbf{b} \equiv 0$). On all four edges of the boundary, we specify zero normal velocities/displacements, that is, homogeneous Dirichlet boundary conditions for the normal velocities/displacements. An example of the displacement magnitude obtained using these parameters is shown in Figure 4c.

Although the exact solution of the problem is smooth, when the classic Galerkin $\mathcal{P}_1/\mathcal{P}_1$ formulation is used, pressure oscillations occur in the nearly incompressible limit (for a Poisson ratio ν approaching 0.5), leading to catastrophic algorithmic failure. We also observed that these pressure oscillations cannot be effectively suppressed by the HFB stabilization. Figure 5 shows a comparison of the pressure error (in this case corresponding to the value of the numerical pressure, since

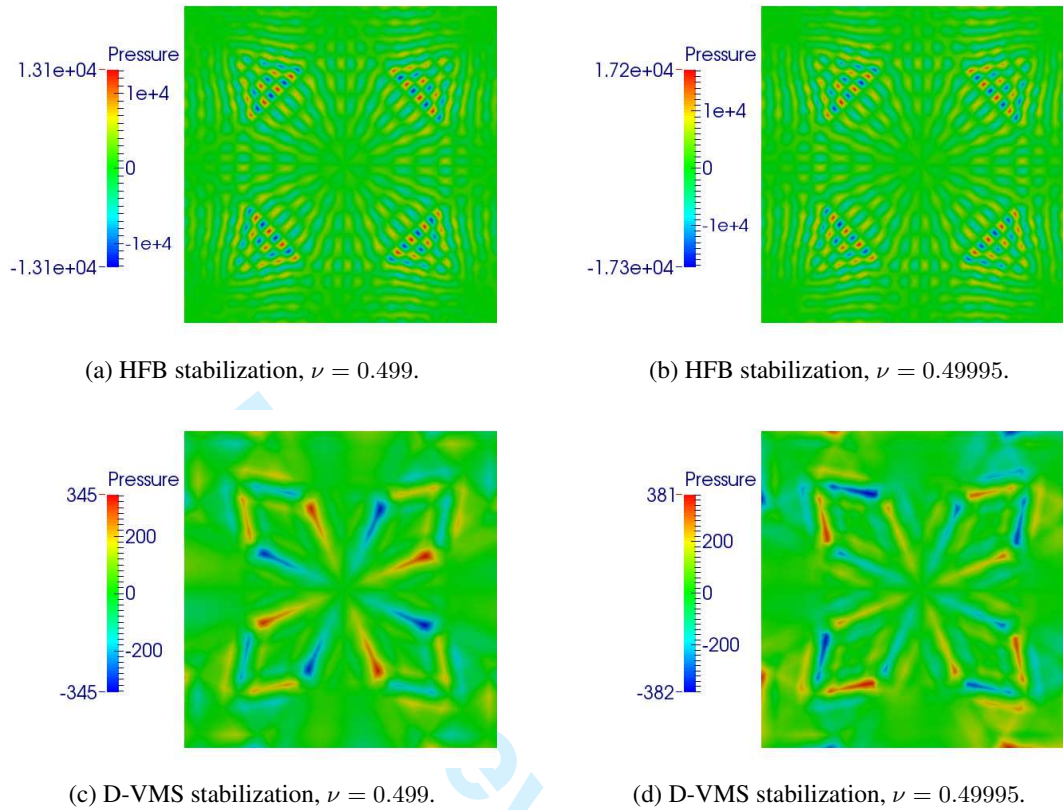


Figure 5. Pressure at $T = 0.01$ for the swinging plate problem computed with the HFB stabilization (upper row) and the D-VMS stabilization (lower row). Two Poisson ratios are used: $\nu = 0.499$ for the plots on the left column, and $\nu = 0.49995$ for the plots on right column. All the computations use a CFL condition $\alpha_{\text{eff}} = 0.9$. Note the accumulation of error in the HFB solution as the Poisson ratio is increased, while the level of error stays stable for the D-VMS approach.

$p^* = 0$) for HFB stabilization with $c_\tau = 0.1$ (value recommended in [12]) and the new proposed D-VMS stabilization with $c_\tau = 0.5$. Computations are performed on a fully unstructured grid of 2,560 triangles and 1,345 nodes, obtained by multiple nested refinements of the grid shown in Figure 4b. It is noticeable that the error in pressure is about two orders of magnitude larger for the HFB stabilization, with respect to the new D-VMS stabilization.

4.2. Two-dimensional swinging plate test II: Convergence of the D-VMS method

Next we studied the convergence behavior of the proposed method by running the previous test on two sequences of seven meshes obtained by refinement of the grids shown in Figures 4a and 4b. The first sequence is of structured grids ranging from 2×8^2 elements (shown in Figure 4a) to 2×512^2 elements. The second sequence is obtained by nested refinements of the grid shown in Figure 4b, with meshes ranging from 40 to 655,360 elements.

To evaluate the performance of the method in the nearly incompressible regime, we consider the cases of Poisson's ratio $\nu = 0.45$ and $\nu = 0.49995$. L_2 -errors of displacement \mathbf{u}^h , velocity \mathbf{v}^h , and pressure p^h at $T = 0.01$ are computed and plotted against the reference element size in logarithmic scale in Figures 6a, 6b, and 6c. We also computed the L_2 -norm of \mathbf{v}' in Figure 6d.

In these plots, we observe second-order convergence rates for the errors in \mathbf{u} and \mathbf{v} , and convergence rates of order 1.5 for the errors in pressure. As already mentioned, although suboptimal, the convergence of the pressure is in any case of higher order than the convergence of the deviatoric

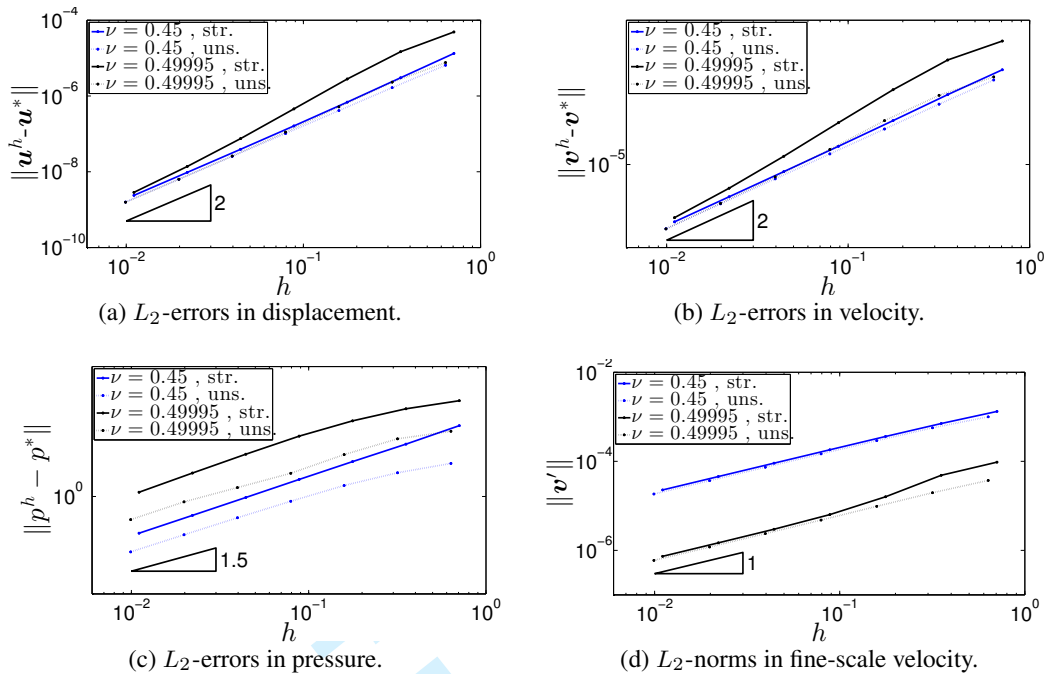


Figure 6. Two-dimensional swinging plate: L_2 -errors for u^h , v^h , p^h , and L_2 -norm of v' . The D-VMS-stabilized method is run with $\tau = c_\tau \alpha_{\text{eff}}^{-1} \Delta t$, $c_\tau = 0.5$, $\alpha_{\text{eff}} = 0.9$. Solid and dashed lines denote the convergence curves for the structured (“str.”) and unstructured meshes (“uns.”), respectively. Blue and black curves denote computations with Poisson ratio $\nu = 0.45$ and $\nu = 0.49995$, respectively.

component of the stress, which is constant over elements and exhibits first-order convergence. This is an important distinction between elasticity and Stokes flow.

In the case of v' , because we use an “incomplete” residual reconstruction, $\|v'\|$ only exhibits first-order convergence, especially when the divergence of the stress deviator is significant (i.e., in the more compressible case, with $\nu = 0.45$). However, note that even if the fine-scale velocity is first order, it does not reduce the order of convergence of the pressure to first order. This is a standard observation for stabilized methods, and was already pointed out in [12].

4.3. Three-dimensional swinging plate test: Additional convergence studies.

The three-dimensional counterpart of the previous test can be obtained by considering a cubic domain $\Omega = [0, 2m]^3$, and an exact displacement law u^* given by

$$u^*(x, t) = U_0 \sin(\omega t) \begin{bmatrix} -2 \sin\left(\frac{\pi}{2}x\right) \cos\left(\frac{\pi}{2}y\right) \cos\left(\frac{\pi}{2}z\right) \\ \cos\left(\frac{\pi}{2}x\right) \sin\left(\frac{\pi}{2}y\right) \cos\left(\frac{\pi}{2}z\right) \\ \cos\left(\frac{\pi}{2}x\right) \cos\left(\frac{\pi}{2}y\right) \sin\left(\frac{\pi}{2}z\right) \end{bmatrix}, \quad (51)$$

where $U_0 = 5 \times 10^{-4}$ m is a constant. Again we set $E = 1.7 \times 10^6$ Pa and $\rho_0 = 1.1 \times 10^3$ kg/m³, $b = 0$, and use the angular frequency ω as

$$\omega = \pi \sqrt{\frac{3\mu}{4\rho_0}}. \quad (52)$$

Homogeneous Dirichlet boundary condition for the normal velocity are applied to all faces of the cubic domain. Also in this case the displacement field is divergence-free, and again $p^* = 0$.

The pattern of the displacement magnitude is depicted in Figure 7c. In the same figure, we also show two sample meshes that are used in the convergence tests.

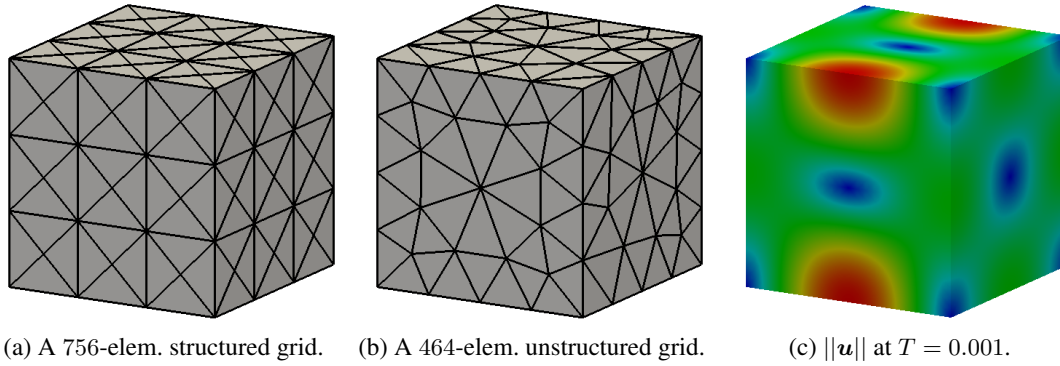


Figure 7. Three-dimensional swinging plate problem: examples of structured and unstructured meshes, and norm of the analytical displacement solution at $T = 0.001$.

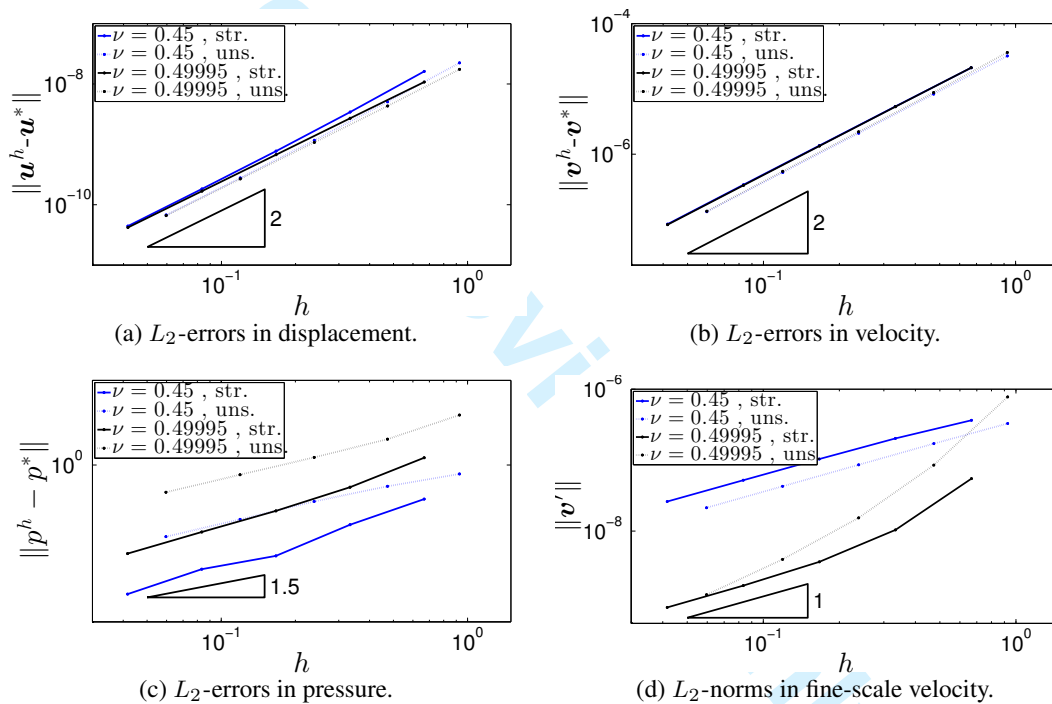


Figure 8. Three-dimensional swinging plate test: L_2 -errors for u^h , v^h , p^h , and L_2 -norm of v' . The D-VMS method is used with $\tau = c_\tau \alpha_{\text{eff}}^{-1} \Delta t$, $c_\tau = 0.15$, $\alpha_{\text{eff}} = 0.9$. The solid and dashed lines denote the convergence curves for the structured ("str.") and unstructured meshes ("uns."), respectively. Blue and black curves are computed using a Poisson ratio $\nu = 0.45$ and $\nu = 0.49995$, respectively.

Figure 7a shows the coarsest of five structured tetrahedral grids with 28×3^3 , 28×6^3 , 28×12^3 , 28×24^3 , and 28×48^3 elements, respectively. These structured grids are generated by first splitting Ω into uniform cubes, and then splitting each cube into 28 tetrahedra. Similarly, Figure 7b shows the coarsest of five unstructured grids of 464, 3,712, 29,696, 237,568, and 1,900,544 elements, respectively. The finer grids are obtained using hierarchical nested grid refinement. L_2 -errors in displacement, velocity, and pressure at $T = 0.001$ are computed and plotted against the reference element size in logarithmic scale in Figures 8a, 8b, and 8c. The L_2 -norm of the fine-scale velocity is plotted in Figure 8d. The results of the three-dimensional version of the swinging plate confirm the results previously discussed in the two-dimensional case: displacement and velocity are second-order, while the pressure converges with order 1.5.

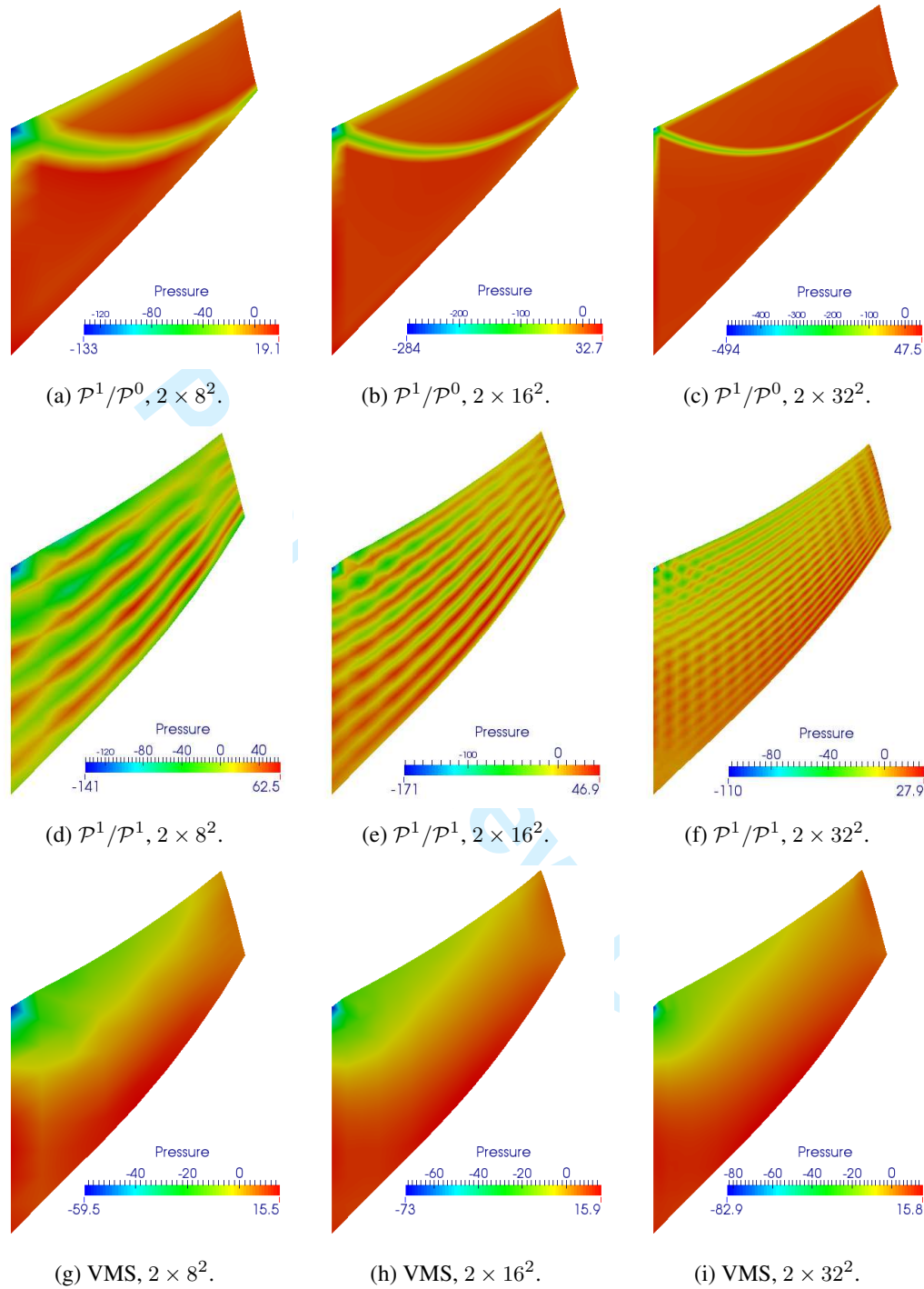


Figure 9. Pressure plot at $T = 10.0$ of the dynamic Cook's membrane test using (9a–9c) the $\mathcal{P}^1/\mathcal{P}^0$ Galerkin formulation with $\alpha_{\text{eff}} = 0.1$, (9d–9f) the $\mathcal{P}^1/\mathcal{P}^1$ Galerkin formulation with $\alpha_{\text{eff}} = 0.1$, and (9g–9i) the D-VMS approach with $\alpha_{\text{eff}} = 0.9$ and stabilization $c_\tau = 0.5$.

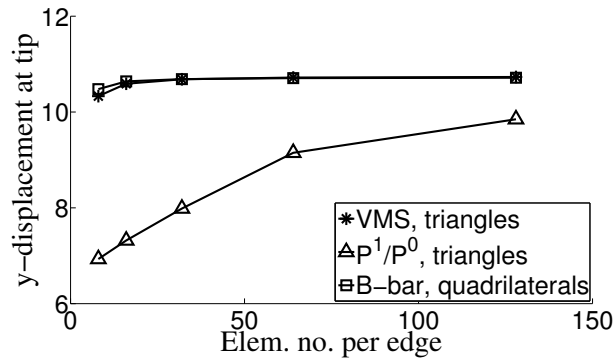


Figure 10. Dynamic Cook's membrane problem: Tip displacement vs. number of elements per edge of the membrane. Comparison between the D-VMS stabilized method with $c_\tau = 0.5$ and the Q^1 B-bar method.

4.4. Dynamic Cook's membrane test, revisited

We return now to the dynamic Cook's membrane test introduced in Section 3.3.4. We evolve in time the solution until $T = 10.0$. As already shown in Section 3.3.4, four structured triangular grids with the number of elements ranging from 2×8^2 to 2×64^2 , the coarsest of which is shown in Figure 1b.

To make the analysis more complete, we also compare the D-VMS solution with a Galerkin method based on P^1/P^0 elements (constant strain element) and a P^1/P^1 formulation without stabilization. We point out that the P^1/P^0 and P^1/P^1 computations could only be run with time steps about an order of magnitude smaller, if compared to the D-VMS method. Namely, we were able to stably run the P^1/P^0 and P^1/P^1 formulations only for $\alpha_{\text{cfl}} = 0.1$ (or lower), while the D-VMS method was run with $\alpha_{\text{cfl}} = 0.9$. As seen in Figures 9a–9c, the P^1/P^0 formulation is affected by severe locking. This is not the case for the P^1/P^1 unstabilized formulation in Figures 9d–9f, which is however affected by pronounced spurious pressure oscillations. The results of the D-VMS simulations are shown in Figures 9g–9i, and demonstrate that the proposed method is stable and converging. More details are presented in Figure 10, where the tip displacement is shown and compared to a computation with the Q^1 B-bar method. From this last plot, it is easier to observe that also the stabilized D-VMS methods is free from locking.

5. NONLINEAR FINITE ELASTICITY

The D-VMS approach can be extended to finite strain hyper-elasticity, by adopting a hydrostatic/deviatoric split of the Helmholtz free energy. We present this strategy next.

5.1. Hyperelasticity model and pressure equation

Consider a nonlinear material with Helmholtz free energy $\Psi(C)$, function of the right Cauchy-Green strain tensor $C = F^T F$. The second Piola-Kirchhoff stress tensor $S = J F^{-1} \sigma F^{-T}$ can be derived by taking derivatives of the Helmholtz free energy functional $\Psi(C)$ with respect to C , namely:

$$S = 2\partial_C \Psi(C). \quad (53)$$

Assuming a volumetric/isochoric decomposition [102] of Ψ , we can write

$$\Psi(C) = U(J) + W(\bar{C}), \quad (54)$$

where $\bar{C} = J^{-2/3} C$ is the deviatoric part of C , and by definition, $J = \sqrt{\det C}$. The definition that we will be using for $U(J)$ and $W(\bar{C})$ is not so important in the discussion to follow, which is indeed quite general, as long as $U(J)$ and $W(\bar{C})$ are uniquely responsible for the elastic energy storage due to volumetric and isochoric (deviatoric) deformation, respectively. A commonly adopted model, is

the neo-hookean material with:

$$U(J) = \frac{1}{4}\kappa(J^2 - 1) - \frac{1}{2}\kappa \ln J, \quad (55a)$$

$$W(\bar{\mathbf{C}}) = \frac{1}{2}\mu(\text{tr } \bar{\mathbf{C}} - 3), \quad (55b)$$

where κ and μ correspond to the bulk modulus and shear modulus, respectively, and are given material constants. In the limit of small displacements, the proposed neo-hookean model collapses to a linearly elastic material. Other models can be considered, and the reader can refer to [103] for alternative definitions, and an in-depth discussion on constitutive model properties and behaviors. The pressure and deviatoric part of the stress can be obtained [102, 104–106] by taking the derivatives:

$$p = U'(J), \quad (56)$$

$$\text{dev}[\boldsymbol{\sigma}] = 2 \frac{W(\bar{\mathbf{C}})}{\partial \bar{\mathbf{C}}} = \mu J^{-5/3} \text{dev}[\mathbf{F} \mathbf{F}^T]. \quad (57)$$

The extension of the VMS method to nonlinear finite hyper-elasticity requires a rate form for the pressure, which can be derived by taking the Lagrangian time derivative of (56). Namely:

$$\dot{p} = U''(J)\dot{J} = U''(J)J \nabla_{\mathbf{x}} \cdot \mathbf{v} = \tilde{\kappa}(J) \nabla_{\mathbf{x}} \cdot \mathbf{v}, \quad (58)$$

where we use the identity $\dot{J} = J \nabla_{\mathbf{x}} \cdot \mathbf{v}$, and

$$\tilde{\kappa}(J) = U''(J)J = \kappa(J + J^{-1})/2. \quad (59)$$

Note that $\tilde{\kappa}(J)$ has the meaning of the *tangent* bulk modulus. The system of equations to be solved is now:

$$\dot{\mathbf{u}} = \mathbf{v}, \quad (60a)$$

$$\rho J = \rho_0, \quad (60b)$$

$$\rho \dot{\mathbf{b}} = \rho \mathbf{b} + \nabla_{\mathbf{x}} p + \nabla_{\mathbf{x}} \cdot (\text{dev}[\boldsymbol{\sigma}]), \quad (60c)$$

$$\dot{p} = \tilde{\kappa}(J) \nabla_{\mathbf{x}} \cdot \mathbf{v}, \quad (60d)$$

where $\text{dev}[\boldsymbol{\sigma}]$ is computed using (57).

5.2. The dynamic VMS approach for transient solid dynamics with finite strain

The variational multi-scale approach in Section 3.4.2 is extended to solve a variational formulation of (60). Without loss of generality and for the sake of simplicity, we assume homogeneous Dirichlet boundary condition on Γ , and use the same trial and test spaces as those given by (16), with the key difference that now the entities Ω , Ω_e , and Γ are associated with the current configuration of the domain/mesh. The variational problem can be cast as:

Seek $\mathbf{u}^h, \mathbf{v}^h \in \mathcal{S}_{\kappa}^h$ and $\rho^h, p^h \in \mathcal{S}_{\gamma}^h$, such that:

$$0 = (\boldsymbol{\psi}^h, \dot{\mathbf{u}}^h - \mathbf{v}^h)_{\Omega}, \quad (61a)$$

$$0 = (\phi^h, \rho^h J - \rho_0)_{\Omega}, \quad (61b)$$

$$0 = (\boldsymbol{\psi}^h, \rho^h \dot{\mathbf{b}}^h)_{\Omega} + (\nabla_{\mathbf{x}} \cdot \boldsymbol{\psi}^h, p^h)_{\Omega} + (\nabla_{\mathbf{x}}^s \boldsymbol{\psi}^h, \boldsymbol{\sigma}^{dev})_{\Omega} - (\boldsymbol{\psi}^h, \rho^h \mathbf{b})_{\Omega}, \quad (61c)$$

$$0 = (\phi^h, \dot{p}^h - \tilde{\kappa}(J) \nabla_{\mathbf{x}} \cdot \mathbf{v}^h)_{\Omega} + (\nabla_{\mathbf{x}} \phi^h, \tilde{\kappa}(J) \mathbf{v}^h)_{\Omega}, \quad (61d)$$

for all $\boldsymbol{\psi}^h \in \mathcal{V}_{\kappa}^h$ and $\phi^h \in \mathcal{V}_{\gamma}^h$.

Algorithm 2 Compute $(\mathbf{u}^{n+1}, \mathbf{v}^{n+1}, \mathbf{p}^{n+1}, \mathbf{p}_n^{n+1})$ from $(\mathbf{u}^n, \mathbf{v}^n, \mathbf{p}^n, \mathbf{p}_n)$ using the predictor/multi-corrector method.

- 1: Retrieve the loop parameter i_{\max} .
- 2: Set $\{\mathbf{u}_{n+1}^{(0)}, \mathbf{v}_{n+1}^{(0)}, \mathbf{p}_{n+1}^{(0)}, \mathbf{p}_n^{(0)}\} = \{\mathbf{u}^n, \mathbf{v}^n, \mathbf{p}^n, \mathbf{p}_n\}$.
- 3: **for** $j = 0, \dots, i_{\max} - 1$ **do**
- 4: Compute τ using (63).
- 5: Assemble $\mathbf{V}_{s;n+1/2}^{(i)}$ and $\mathbf{M}_{v;n+1/2}^{(i)}$.
- 6: Assemble $\mathbf{W}_{n+1/2}^{(i)}$.
- 7: Pressure update: $\mathbf{p}_{n+1}^{(i+1)} = \mathbf{p}_n - \Delta t_n [\mathbf{V}_{s;n+1/2}^{(i)}]^{-1} \mathbf{W}_{n+1/2}^{(i)}$.
- 8: Assemble $\mathbf{F}_{n+1/2}^{(i,i+1)}$.
- 9: Velocity update: $\mathbf{v}_{n+1}^{(i+1)} = \mathbf{v}_n - \Delta t_n [\mathbf{M}_{v;n+1/2}^{(i)}]^{-1} \mathbf{F}_{n+1/2}^{(i,i+1)}$.
- 10: Displacement update: $\mathbf{u}_{n+1}^{(i+1)} = \mathbf{u}_n + \Delta t_n \mathbf{v}_{n+1/2}^{(i+1)}$.
- 11: Assemble $\mathbf{V}_{s;n+1}^{(i+1)}$.
- 12: Density update: $\mathbf{p}_{n+1}^{(i+1)} = [\mathbf{V}_{s;n+1}^{(i+1)}]^{-1} \mathbf{M}_0$.
- 13: **end for**
- 14: Set $(\mathbf{u}^{n+1}, \mathbf{v}^{n+1}, \mathbf{p}^{n+1}, \mathbf{p}_n^{n+1}) = (\mathbf{u}_{n+1}^{(i_{\max})}, \mathbf{v}_{n+1}^{(i_{\max})}, \mathbf{p}_{n+1}^{(i_{\max})}, \mathbf{p}_n^{(i_{\max})})$.
- 15: Compute Δt^{n+1} using (69).

Similar to the linear case, the fine-scale velocity *ansatz* is proposed as a scaled residual in the current configuration, namely:

$$\mathbf{v}' = -\frac{\tau}{\rho^h} (\rho^h \dot{\mathbf{v}}^h - \nabla_{\mathbf{x}} p^h - \nabla_{\mathbf{x}} \cdot \boldsymbol{\sigma}^{dev} - \rho^h \mathbf{b}) , \quad (62)$$

and

$$\tau = \frac{c_{\tau}}{\alpha_{\text{cfl}}} \Delta t , \quad \text{or} \quad \tau = \frac{c_{\tau} h^e}{\sqrt{(\tilde{\kappa} + 3\mu/4)/\rho^h}} . \quad (63)$$

Remark 12. Because $\boldsymbol{\sigma}^{dev}$ is a constant within each element, the third term of (62) vanishes and it leads to an “incomplete” residual for the velocity, as in the linear elasticity case.

The finite strain assumption implies that the trial and test spaces in (16) vary with time, as the domain deforms. Therefore, the shape functions are defined through the motion (or deformation) map, as shown momentarily in Section 5.3.

5.3. Implementation of the dynamic VMS algorithm

The \mathcal{P}^1 approximations to the solution variables at a time instance t_n reads

$$\mathbf{u}_n = \sum_{A=1}^{n_{np}} N_{A;n} \mathbf{u}_{A;n} , \quad \rho_n = \sum_{A=1}^{n_{np}} N_{A;n} \rho_{A;n} , \quad \mathbf{v}_n = \sum_{A=1}^{n_{np}} N_{A;n} \mathbf{v}_{A;n} , \quad p_n = \sum_{A=1}^{n_{np}} N_{A;n} p_{A;n} . \quad (64)$$

Note that the shape functions are associated with the mesh configuration \mathbf{x}_n . Since we are in the framework of isoparametric elements, the shape functions can be expressed in terms of the deformation map:

$$N_{A;n}(\boldsymbol{\varphi}(\mathbf{X}, t_n)) = N_{0;A}(\mathbf{X}) , \quad (65)$$

where $N_{0;A}$ is the shape function associated with node \mathbf{X}_A at the initial mesh configuration, and $\boldsymbol{\varphi}$ is affine on each element $\Omega_{0;e}$.

Similar to Section 3, we use the predictor/multi-corrector algorithm for integration in time, and mass lumping for all solution updates. In particular, let \mathbf{M}_n be the vector of nodal mass at t_n :

$$\mathbf{M}_n = [\mathbf{M}_{n;A}] , \quad \mathbf{M}_{n;A} = (N_{n;A}, \rho_n) \Omega_n , \quad (66)$$

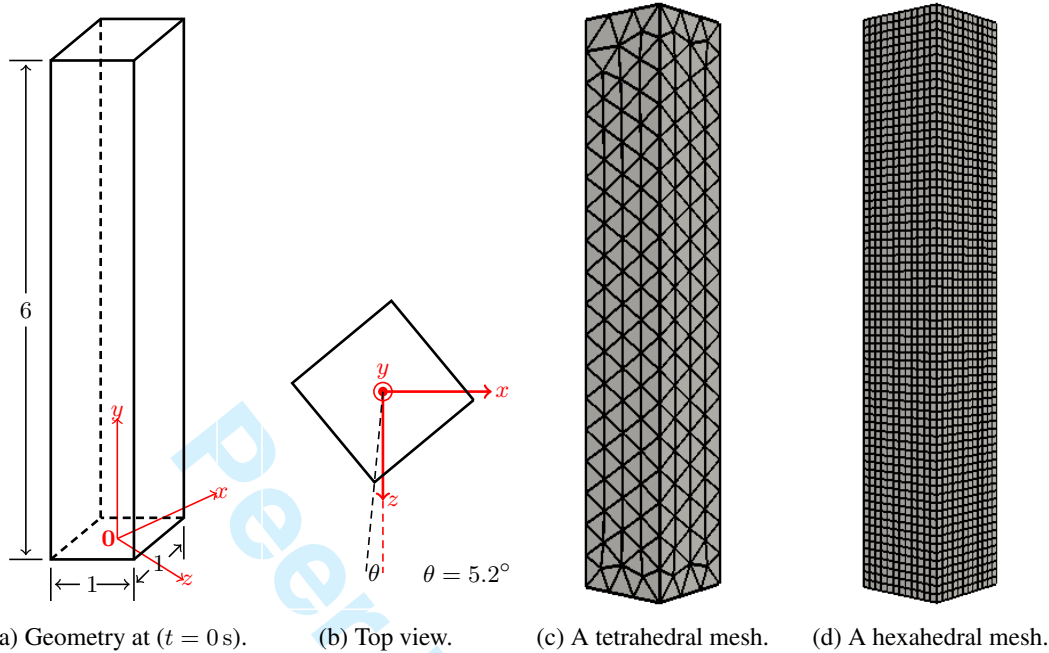


Figure 11. A beam bending problem: The geometric setup of the beam in its initial configuration is shown in Figure (11a). The initial velocity is along the x -axis shown in the top view of Figure (11b). Figure (11c) shows an unstructured mesh with 1,775 tetrahedral elements, while Figure (11d) shows a $12 \times 12 \times 72$ hexahedral mesh, used to compute a reference solution.

the lumped mass matrix is $\mathbf{M}_{v;n} = [\text{diag}(\mathbf{M}_n, \mathbf{M}_n, \mathbf{M}_n)]$. Similarly, let \mathbf{V}_n be the vector of nodal volumes at t_n , that is

$$\mathbf{V}_n = [\mathbf{V}_{n;A}], \quad \mathbf{V}_{n;A} = (N_{n;A}, 1)_{\Omega_n}, \quad (67)$$

the lumped volume matrix is $\mathbf{V}_{s;n} = [\text{diag}(\mathbf{V}_n)]$. Using these notations, the variational forms (61a–61d) lead to the following matrix forms:

$$\mathbf{V}_{s;n+1/2}^{(i)} \frac{\mathbf{p}_{n+1}^{(i+1)} - \mathbf{p}_n}{\Delta t_n} = -\mathbf{W}_{n+1/2}^{(i)}, \quad (68a)$$

$$\mathbf{M}_{v;n+1/2}^{(i)} \frac{\mathbf{v}_{n+1}^{(i+1)} - \mathbf{v}_n}{\Delta t_n} = -\mathbf{F}_{n+1/2}^{(i,i+1)}, \quad (68b)$$

$$\frac{\mathbf{u}_{n+1}^{(i+1)} - \mathbf{u}_n}{\Delta t_n} = \mathbf{v}_{n+1/2}^{(i+1)}, \quad (68c)$$

$$\mathbf{p}_{n+1}^{(i+1)} = [\mathbf{V}_{s;n+1}^{(i+1)}]^{-1} \mathbf{M}_0. \quad (68d)$$

Here $i = 0, \dots, i_{\max}$ and $i_{\max} = 3$ is used for all numerical examples. The vector $\mathbf{W}_{n+1/2}^{(i)}$ is computed according to (61d) using:

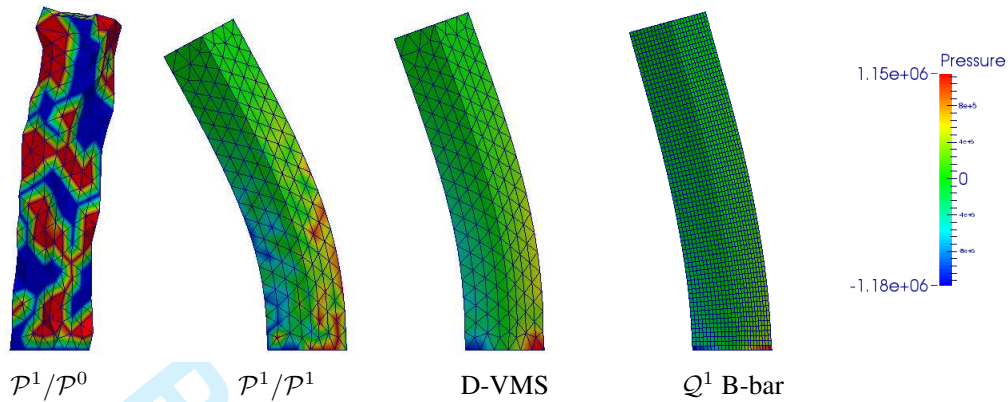
$$J = J(\mathbf{u}_{n+1/2}^{(i)}), \quad \mathbf{x}_{n+1/2}^{(i)} = \mathbf{X} + \mathbf{u}_{n+1/2}^{(i)}, \quad \mathbf{v}^h = \mathbf{v}_{n+1/2}^{(i)},$$

and $\mathbf{v}' = -\frac{\tau}{\rho_{n+1/2}^{(i)}} \left(\rho_{n+1/2}^{(i)} \frac{\mathbf{v}_{n+1}^{(i)} - \mathbf{v}_n}{\Delta t_n} - \nabla \cdot \mathbf{x} p_{n+1/2}^{(i)} - \rho_{n+1/2}^{(i)} \mathbf{b}_{n+1/2} \right), \quad (68e)$

and $\mathbf{F}_{n+1/2}^{(i,i+1)}$ is computed according to (61c) using:

$$\rho^h = \rho_{n+1/2}^{(i)}, \quad p^h = p_{n+1/2}^{(i+1)}, \quad \mathbf{x}_{n+1/2}^{(i)} = \mathbf{X} + \mathbf{u}_{n+1/2}^{(i)}, \quad J = J(\mathbf{u}_{n+1/2}^{(i)}).$$

Deformation with pressure contours at $t = 1.0$ s.



Deformation with pressure contours at $t = 2.0$ s.

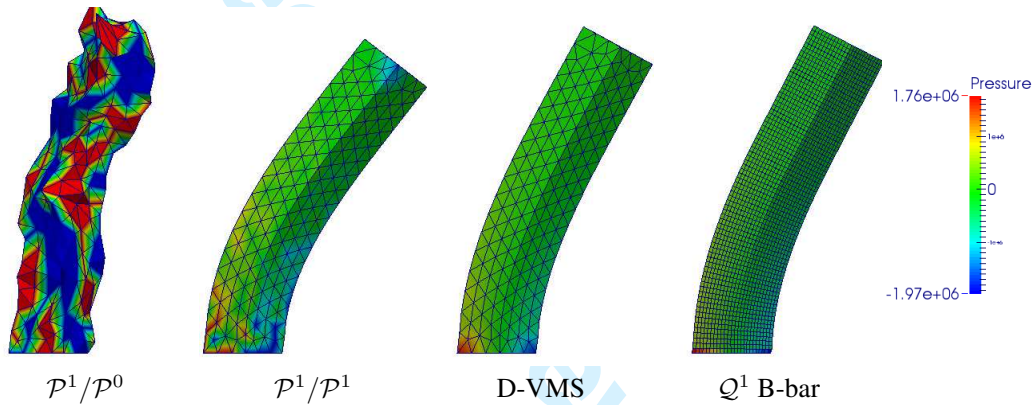


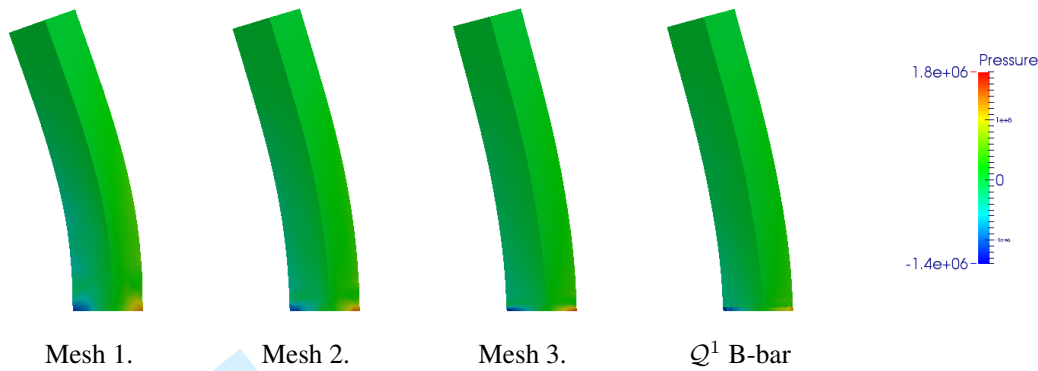
Figure 12. Bending beam test: Pressure at $t = 1.0$ s (upper row) and $t = 2.0$ s (lower row) for a coarse mesh with 1,775 elements. From the left to the right: $\mathcal{P}^1/\mathcal{P}^0$ mixed Galerkin method, $\mathcal{P}^1/\mathcal{P}^1$ mixed Galerkin method without stabilization, D-VMS with mixed $\mathcal{P}^1/\mathcal{P}^1$ elements and $c_\tau = 0.15$, and the \mathcal{Q}^1 B-bar finite element method (reference). All computations were performed with the CFL number $\alpha_{\text{cfl}} = 0.9$.

All the previous computational steps are summarized in Algorithm 2. The new time step Δt^{n+1} is computed using the updated bulk wave speed and reference element length:

$$\Delta t_{n+1} = \alpha_{\text{cfl}} \min_{\Omega_e \subset \Omega_{n+1}} \frac{h_e}{(\sqrt{\tilde{\kappa}(J_{n+1})} + 3\mu/4)/\rho_{n+1}}. \quad (69)$$

Remark 13. In principle, the computation of Δt must be incorporated into the inner loop of the predictor/multi-corrector procedure, as both the element length and bulk wave speed may change with the corrector iterates. However, since these quantities do not change by much between iterates, we freeze the time-step size during the correction stages and choose a CFL number $\alpha_{\text{cfl}} = 0.9$ not too close to 1 as a safeguard procedure. Our experience indicates that $\alpha_{\text{cfl}} = 0.9$ leads to robust computations, and is our preferred value.

Deformation with pressure contours at $t = 1.0$ s.



Deformation with pressure contours at $t = 2.0$ s.

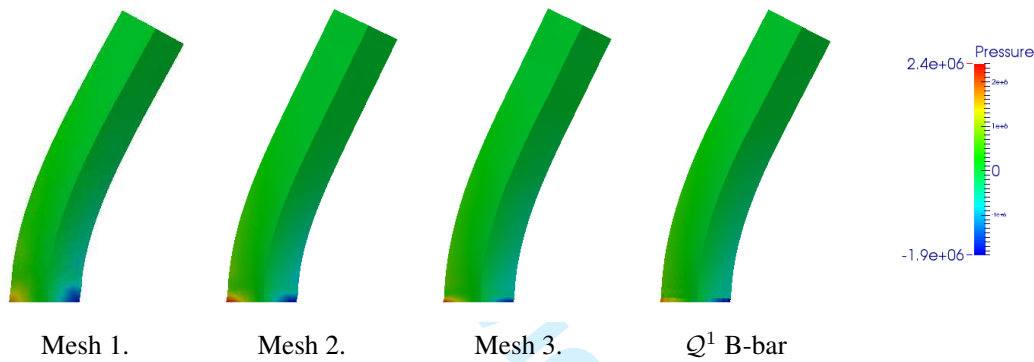


Figure 13. Pressure contours and deformation for the beam bending problem with $\nu = 0.499$. Three levels of grid refinement (left three columns) are used in combination with the D-VMS described in Section 5. The fourth column shows the reference results using Q^1 B-bar method with hexahedral elements. Solutions at $t = 1.0$ and $t = 2.0$ are plotted on the upper and lower row respectively. The D-VMS uses $c_\tau = 0.15$ and the CFL number $\alpha_{\text{cfl}} = 0.9$.

6. NUMERICAL RESULTS: FINITE ELASTICITY

6.1. A bending beam test

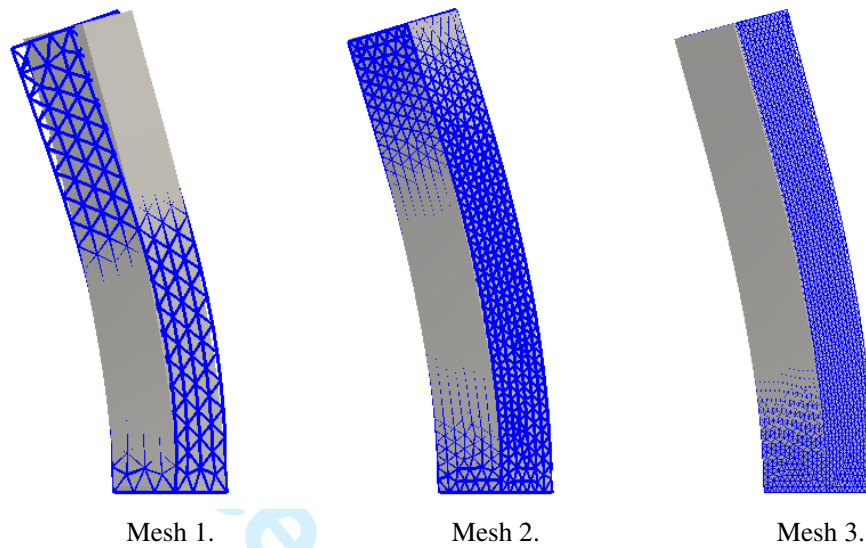
As a first test in finite elasticity, we select a bending problem for a beam-like structure of square section. The initial geometry is very similar to one presented in [46, 47]: The beam is a parallelepiped of dimension $1 \text{ m} \times 1 \text{ m} \times 6 \text{ m}$, as shown in Figure 11a. Our version of the test slightly differs from the one described in [46, 47], in that the beam is rotated by an angle $\theta = 5.2^\circ$ about the z -axis, to avoid symmetries in the problem.

Initially, the beam is stress free, and zero displacement initial conditions ($\mathbf{u}(\mathbf{x}, 0) = \mathbf{0} \text{ m}$) are applied. Bending is initiated through the velocity initial condition:

$$\mathbf{v}(\mathbf{x}, 0) = \mathbf{v}(x, y, z, 0) = \{5/3 y, 0.0, 0.0\}^T \text{ m/s}, \quad y \in [0, 6] \text{ m}, \quad (70)$$

where the origin of the coordinate system is at the center of the square base section of the beam (as shown in Figures 11a and 11b). The material is neo-Hookean with parameters $\rho_0 = 1.1 \times 10^3 \text{ kg/m}^3$, $E = 1.7 \times 10^7 \text{ Pa}$, and Poisson ratio is $\nu = 0.499$. The bulk and shear moduli are computed from E and ν using (9), which nominally pertains to the linearized theory of elasticity, but is also assumed to hold in this case. We enforce homogeneous boundary condition for \mathbf{u} and \mathbf{v} on the bottom, and all other boundary conditions are specified by zero tractions.

Deformation comparison at $t = 1.0$ s.



Deformation comparison at $t = 2.0$ s.

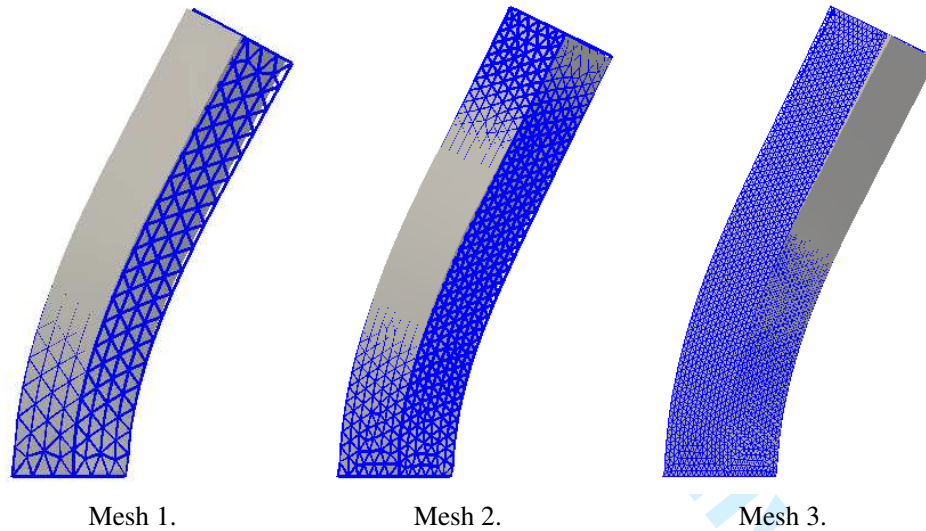


Figure 14. Deformation solution for the beam bending problem with $\nu = 0.499$ on three level of refinement for the D-VMS approach. The solution using the VMS approach (blue grid) is overlapped with the reference Q^1 B-bar solution (in gray). Solutions at $t = 1.0$ and $t = 2.0$ are plotted on the upper and lower row respectively. The D-VMS uses $c_\tau = 0.15$ and the CFL number $\alpha_{\text{cfl}} = 0.9$.

We computed the solutions until $T = 2.0$ s using four different methods: (a) the $\mathcal{P}^1/\mathcal{P}^0$ mixed Galerkin method (equivalent to using linear finite elements for the displacements); (b) the $\mathcal{P}^1/\mathcal{P}^1$ mixed Galerkin method without stabilization; (c) the D-VMS stabilized mixed method proposed in Section 5.2 (with $\mathcal{P}^1/\mathcal{P}^1$ approximation spaces); and (d) the Q^1 B-bar hexahedral element. Computations with the first three methods are performed on unstructured tetrahedral meshes analogous to the one in Figure 11c, while the reference solution is computed on the structured hexahedral mesh depicted in Figure 11d.

Figure 12 shows the deformation and pressure color plot at the instants $t = 1.0$ s and $t = 2.0$ s. It is easy to observe that:

1. The mixed Galerkin method with $\mathcal{P}^1/\mathcal{P}^0$ interpolation is affected by severe volumetric locking, massive pressure oscillations, and spurious deformation modes. As expected, for all practical purposes, the computational results are useless.
2. The mixed Galerkin method with $\mathcal{P}^1/\mathcal{P}^1$ interpolation suffers from large pressure oscillations, predominant near the base and the tip of the beam.
3. The D-VMS method produces the most accurate solutions in terms of displacements, and the pressures stay smooth throughout the computation. Accuracy is measured by comparing the D-VMS solution with the solution of the \mathcal{Q}^1 B-bar method using a much finer grid of $12 \times 12 \times 72$ hexahedral elements.

These observations help us conclude that the D-VMS stabilized method is the best performer on tetrahedral grids in the incompressible limit. We also performed a mesh refinement study for the same problem, as often time instability in finite element formulations which are not LBB-stable become more intense as grids are refined. For this purpose we considered the solution of the D-VMS approach on three unstructured tetrahedral meshes with 1,775, 11,575, and 84,042 elements, respectively.

It is easily appreciated from the plots of Figure 13 that for resolution equal or finer than the second mesh, the stabilized method is almost identical to the reference solution. In Figure 14, we overlap the reference solution in gray, and the D-VMS solution grid deformation in blue. It becomes even more clear that starting on moderately coarse grids, the tetrahedral finite element computations using the D-VMS approach deliver results difficult to tell apart from the reference hexahedral solution.

6.2. The twisting column test

The last example we present is a twisting column test [44, 54]. The geometry and material properties are identical to the bending problem described in the previous section. The initial configuration of the column is shown in Figure 11a and the initial displacements are zero (in other words, there is no preload on the solid). The twisting motion is applied to the column by means of the following initial condition on the velocity:

$$\mathbf{v}(\mathbf{x}, 0) = \mathbf{v}(x, y, z, 0) = 100 \sin\left(\frac{\pi y}{12}\right) \{z, 0.0, -x\}^T \text{ m/s}, \quad y \in [0, 6] \text{ m}. \quad (71)$$

The directions and magnitudes of the velocity initial conditions are depicted using red curves in the sketch of Figure 15a. Velocity homogeneous Dirichlet boundary conditions are applied at the bottom of the column, which is therefore clamped, and homogeneous Neumann boundary conditions are used on all the other sides of the column (stress-free conditions).

Because of the inherent symmetries in the geometry of the problem, we initially consider tetrahedral grids obtained by constructing first hexahedral grids similar to the one in Figure 11d and subsequently splitting each hexahedral element into six tetrahedra, as shown in Figure 15b. This meshing strategy was also explored in [44, 54], and an example of the resulting grids is shown in Figure 15c. In the computations presented, we consider two levels of refinement, that is, meshes with $6 \times 6 \times 36$ and $12 \times 12 \times 72$ hexahedral elements (further subdivided into tetrahedra). We denote these two meshes by M1 and M2, respectively, in the figures to follow. We also use an additional unstructured tetrahedral grid, denoted M2U, with resolution comparable to the M2 grid. The M2U mesh fills the space more evenly than the grid M2 - its elements being on average less distorted - and will be shown to yield improved results. The various combinations of methods and grids used to compute numerical solutions are summarized in Table I.

Deformation and pressure contours for this test are plotted at time instants $t = 0.1 \text{ s}$, 0.2 s , 0.3 s , and 0.4 s in Figures 16, 17, 18, and 19, respectively. The Galerkin $\mathcal{P}^1/\mathcal{P}^0$ formulation fails to deliver a solution in this problem, and for this reason, is omitted from the plots.

From Figures 16–19, it is easy to observe that without stabilization, the $\mathcal{P}^1/\mathcal{P}^1$ mixed finite element formulation produces large oscillations. This is not the case for the D-VMS method, which produces oscillation-free solutions, in very good agreement with computations using \mathcal{Q}^1 B-bar

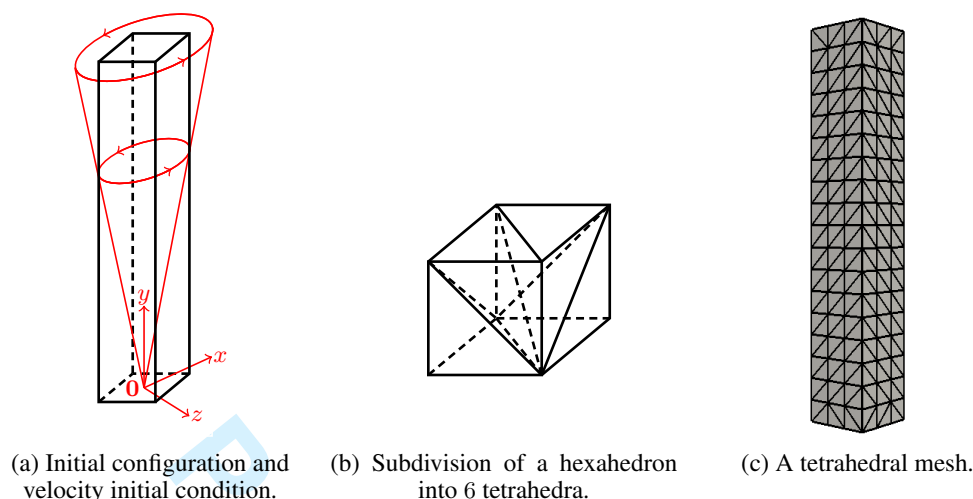


Figure 15. Setup and grids used for the twisting column problem.

Table I. Numerical methods involved in computing the solutions in Figures 16–19.

Abbreviation	Description of numerical method
$\mathcal{P}^1/\mathcal{P}^1$, M1	Mixed $\mathcal{P}^1/\mathcal{P}^1$ Galerkin using the coarse M1 mesh (tetrahedral subdivision)
D-VMS, M1	D-VMS method using the coarse M1 mesh (tetrahedral subdivision)
D-VMS, M2	D-VMS method using the coarse M2 mesh (tetrahedral subdivision)
D-VMS, M2U	D-VMS method using the finer fully unstructured M2U mesh
\mathcal{Q}^1 B-bar, M2	B-bar/selective integration method using the M2 mesh (hexahedral elements)

elements on grids of similar resolution. In Figure 20 we overlapped the solution using the D-VMS approach on tetrahedral finite elements (blue grids) with the reference solution using a B-bar method and hexahedral finite elements (solid gray). In these plots, it is easy to appreciate that the solution with tetrahedral finite elements on the unstructured grid M2U is very close to (and at times perfectly matched with) the B-bar solution, on a grid of analogous resolution. We think that this result is remarkable, considering that the twisting column test is challenging already from the point of view of robustness.

7. CONCLUSIONS AND FUTURE DIRECTIONS

We presented a new stabilized finite element method - which we denoted Dynamic VMS - for nearly incompressible linear and nonlinear elastic computations on tetrahedral grids with piecewise linear interpolation spaces. The proposed method is based on a mixed velocity-pressure formulation with equal order (linear) interpolation. We showed with a variety of computational tests that the D-VMS method is very similar in performance to the \mathcal{Q}^1 B-bar hexahedral element. In developing this new method, we discovered the limitations of previous stabilized methods initially targeted at static incompressible elasticity. We attributed this lack of performance to the different structure of the elasticity operators in the static (elliptic partial differential equations) and dynamic (hyperbolic partial differential equations) cases. We also observed that the proposed stabilizing mechanism accounts for the accumulation of the fine-scales effects into the coarse scale equation over time, and we attribute to this feature the greatly improved performance. We are in the process of completing the development of implicit time integration strategies, and to extend the proposed methodologies to linear and nonlinear viscoelastic computations. We hope to report soon on both fronts of our current investigations.

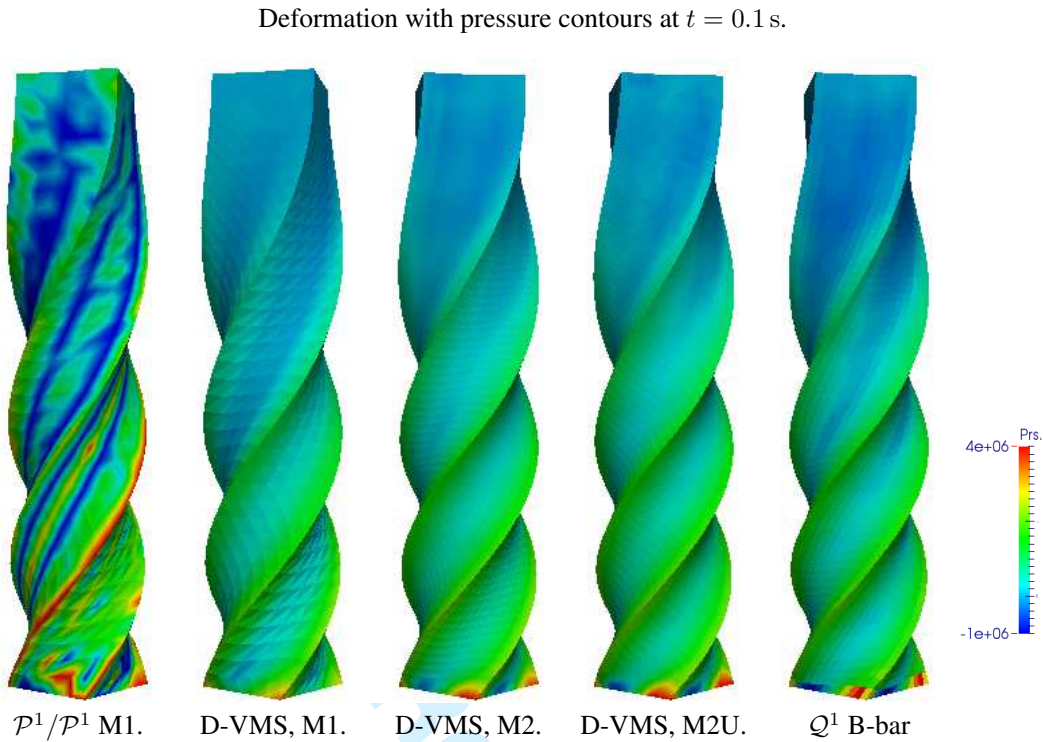


Figure 16. Deformation and pressure contours for the twisting column test with $\nu = 0.499$ at $t = 0.1$ s. D-VMS computations were performed with $\alpha_{\text{eff}} = 0.9$ and $c_\tau = 0.15$.

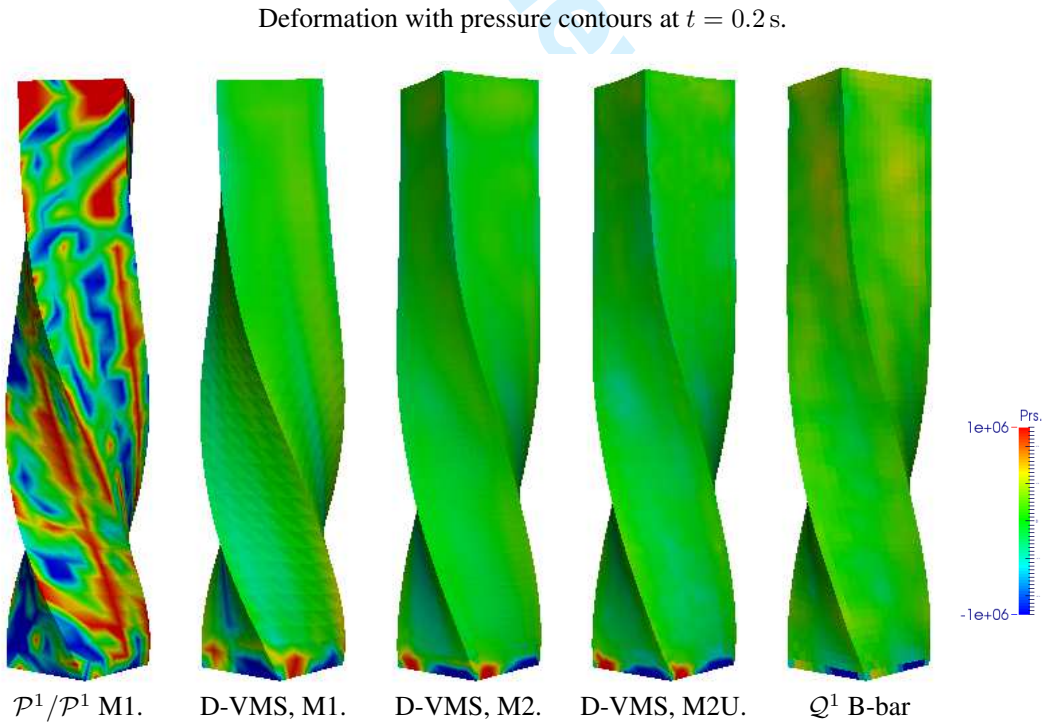


Figure 17. Deformation and pressure contours for the twisting column test with $\nu = 0.499$ at $t = 0.2$ s. D-VMS computations were performed with $\alpha_{\text{eff}} = 0.9$ and $c_\tau = 0.15$.

Deformation with pressure contours at $t = 0.3$ s.

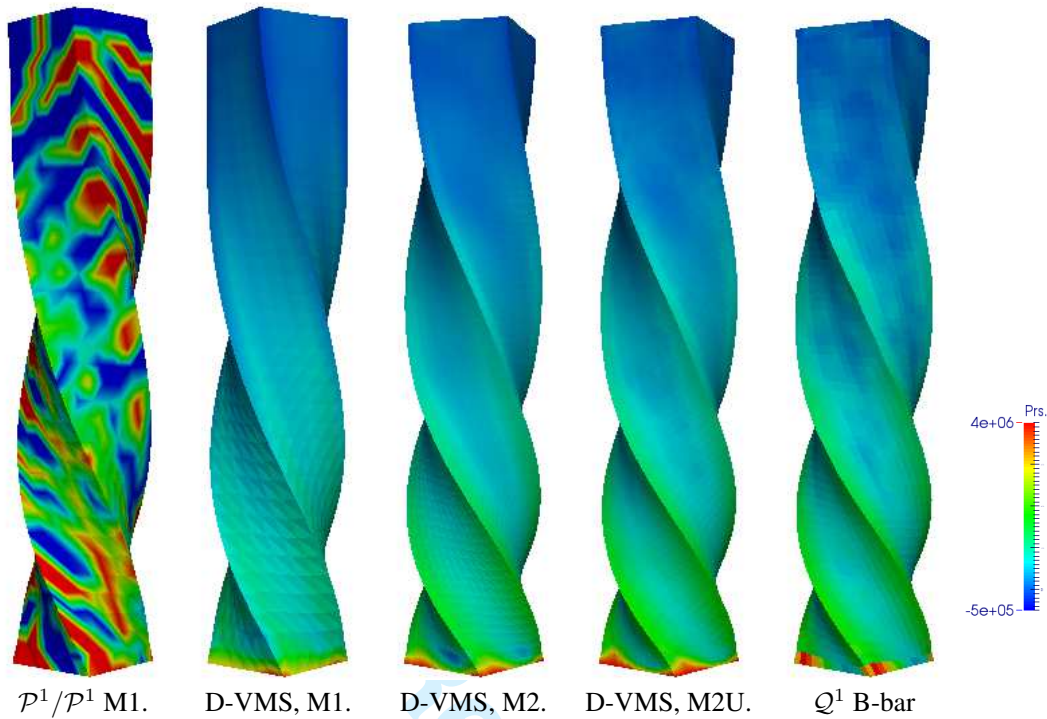


Figure 18. Deformation and pressure contours for the twisting column test with $\nu = 0.499$ at $t = 0.3$ s. D-VMS computations were performed with $\alpha_{\text{eff}} = 0.9$ and $c_\tau = 0.15$.

Deformation with pressure contours at $t = 0.4$ s.

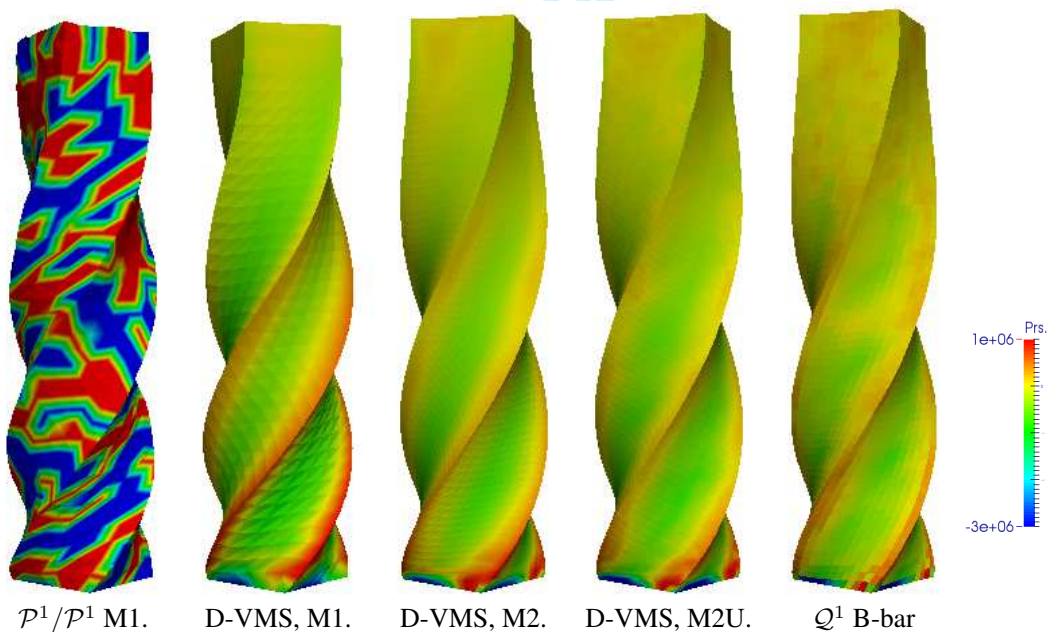


Figure 19. Deformation and pressure contours for the twisting column test with $\nu = 0.499$ at $t = 0.4$ s. D-VMS computations were performed with $\alpha_{\text{eff}} = 0.9$ and $c_\tau = 0.15$.

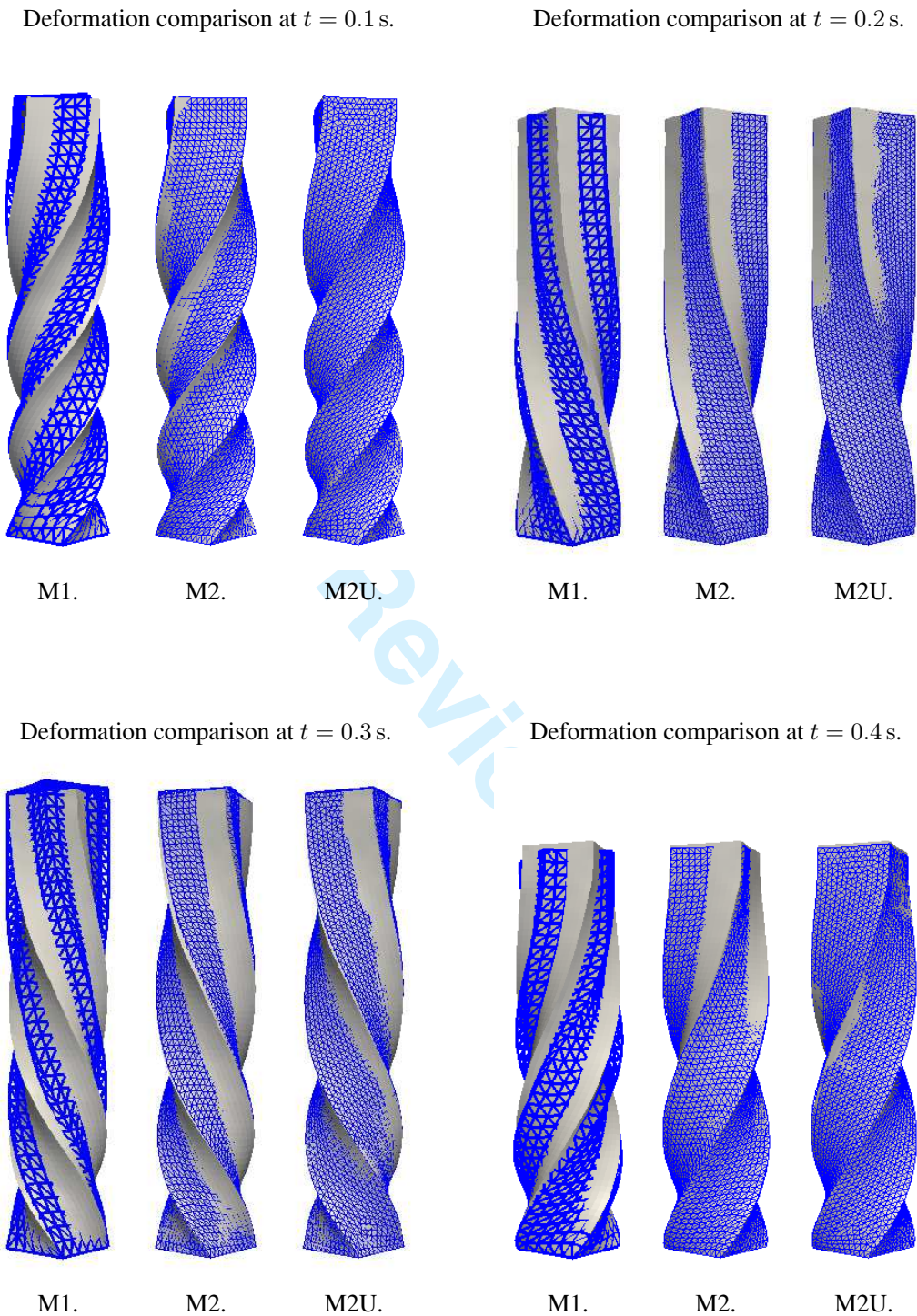


Figure 20. Deformation solution for the twisting column test with $\nu = 0.499$ on three types of grids for the D-VMS approach. The solution using the VMS approach (blue grid) is overlapped with the baseline reference solution using a selective integration/B-bar strategy (in gray). Solutions at $t = 0.1$, $t = 0.2$, $t = 0.3$, and $t = 2.0$ are plotted in sequence. The D-VMS uses $c_\tau = 0.15$ and the CFL number $\alpha_{\text{cfl}} = 0.9$.

ACKNOWLEDGMENTS

The first and third of the authors acknowledge the support of the Computer Science Research Institute at Sandia National Laboratories, the U.S. Office of Naval Research under grant N00014-14-1-0311, and the U.S. Department of Energy, Office of Science, Advanced Scientific Computing Research under grant SC0012169. Sandia National Laboratories is a multi-program laboratory operated by Sandia Corporation, a wholly owned subsidiary of Lockheed Martin company, for the U.S. Department of Energy's National Nuclear Security Administration under contract DE-AC04-94AL85000.

REFERENCES

- [1] Hughes TJR. *The Finite Element Method: Linear Static and Dynamic Finite Element Analysis*. Prentice-Hall: Englewood Cliffs, New Jersey, 1987. (Dover reprint, 2000).
- [2] Hughes TJR. Equivalence of finite elements for nearly incompressible elasticity. *J. Appl. Mech., Trans. ASME* 1977; **44**(1):181–183.
- [3] Hughes TJR. Generalization of selective integration procedure to anisotropic and nonlinear media. *Int. J. Numer. Meth. Eng.* 1980; **15**(1):1413–1418.
- [4] de Souza Neto EA, Andrade Pires FM, Owen DRJ. F-bar-based linear triangles and tetrahedra for finite strain analysis of nearly incompressible solids. Part I: Formulation and benchmarking. *Int. J. Numer. Meth. Eng.* 2005; **62**(3):353–383.
- [5] de Souza Neto EA, Perić D, Huang GC, Owen DRJ. Remarks on the stability of enhanced strain elements in finite elasticity and elastoplasticity. *Comm. Numer. Meth. Eng.* 1995; **11**(11):951–961.
- [6] De Souza Neto EA, Perić D, Dutko M, Owen DRJ. Design of simple low order finite elements for large strain analysis of nearly incompressible solids. *Int. J. Solids Struct.* 1996; **33**(20–22):3277–3296.
- [7] Nagtegaal JC, Park DM, Rice JR. On numerically accurate finite element solutions in the fully plastic range. *Comput. Methods Appl. Mech. Eng.* 1974; **4**:53–177.
- [8] Babuška I. Error-bounds for finite element method. *Numer. Math.* 1971; **16**(4):322–333.
- [9] Brezzi F, Fortin M. *Mixed and Hybrid Finite Element Methods*, Springer Series in Computational Mathematics, vol. 15. 1 edn., Springer New York, 1991.
- [10] Ern A, Guermond JL. *Theory and Practice of Finite Elements*, Applied Mathematical Sciences, vol. 159. Springer New York, 2004.
- [11] Malkus DS, Hughes TJR. Mixed finite element methods - reduced and selective integration techniques: A unification of concepts. *Comput. Methods Appl. Mech. Eng.* 1978; **15**(1):68–81.
- [12] Hughes TJR, Franca LP, Balestra M. A new finite element formulation for computational fluid dynamics: V. Circumventing the Babuška-Brezzi condition: A stable Petrov–Galerkin formulation of the Stokes problem accommodating equal-order interpolations. *Comput. Methods Appl. Mech. Eng.* November 1986; **59**(1):85–99.
- [13] Hughes TJR, Franca LP. A new finite element formulation for computational fluid dynamics: VII. The Stokes problem with various well-posed boundary conditions: Symmetric formulations that converge for all velocity/pressure spaces. *Comput. Methods Appl. Mech. Eng.* 1987; **65**(1):85 – 96.

- [14] Franca LP, Hughes TJR. Two classes of mixed finite element methods. *Comput. Methods Appl. Mech. Eng.* 1988; **69**(1):89 – 129.
- [15] Franca LP, Hughes TJR, Loula AFD, Miranda I. A new family of stable elements for nearly incompressible elasticity based on a mixed Petrov-Galerkin finite element formulation. *NM* 1988; **53**(1–2):123–141.
- [16] Klaas O, Maniatty A, Shephard MS. A stabilized mixed finite element method for finite elasticity. Formulation for linear displacement and pressure interpolation. *Comput. Methods Appl. Mech. Eng.* November 1999; **180**(1–2):65–79.
- [17] Maniatty AM, Liu Y, Klaas O, Shephard MS. Stabilized finite element method for viscoplastic flow: formulation and a simple progressive solution strategy. *Comput. Methods Appl. Mech. Eng.* June 2001; **190**(35–36):4609–4625.
- [18] Maniatty AM, Liu Y, Klaas O, Shephard MS. Higher order stabilized finite element method for hyperelastic finite deformation. *Comput. Methods Appl. Mech. Eng.* January 2002; **191**(13–14):1491–1503.
- [19] Maniatty AM, Liu Y. Stabilized finite element method for viscoplastic flow: formulation with state variable evolution. *Int. J. Numer. Meth. Eng.* January 2003; **56**(2):185–209.
- [20] Ramesh B, Maniatty AM. Stabilized finite element formulation for elastic–plastic finite deformations. *Comput. Methods Appl. Mech. Eng.* 2005; **194**(6–8):775–800.
- [21] Masud A, Xia K. A stabilized mixed finite element method for nearly incompressible elasticity. *J. Appl. Mech.* January 2005; **72**(5):711–720.
- [22] Nakshatrala K, Masud A, Hjelmstad K. On finite element formulations for nearly incompressible linear elasticity. *Comput. Mech.* 2008; **41**(4):547–561.
- [23] Xia K, Masud A. A stabilized finite element formulation for finite deformation elastoplasticity in geomechanics. *Comput. Geotech.* 2009; **36**(3):396–405.
- [24] Masud A, Truster TJ. A framework for residual-based stabilization of incompressible finite elasticity: Stabilized formulations and methods for linear triangles and tetrahedra. *Comput. Methods Appl. Mech. Eng.* 2013; **267**:359–399.
- [25] Hughes TJR. Multiscale phenomena: Green's functions, the Dirichlet-to-Neumann formulation, subgrid scale models, bubbles and the origins of stabilized methods. *Comput. Methods Appl. Mech. Eng.* November 1995; **127**(1–4):387–401.
- [26] Hughes TJR, Feijóo GR, Mazzei L, Quincy JB. The variational multiscale method – a paradigm for computational mechanics. *Comput. Methods Appl. Mech. Eng.* November 1998; **166**(1–2):3–24.
- [27] Hughes TJR, Scovazzi G, P FL. Multiscale and stabilized methods. *Encyclopedia of Computational Mechanics*, Stein E, de Borst R, Hughes TJR (eds.). John Wiley & Sons, 2004.
- [28] Chiumenti M, Valverde Q, de Saracibar CA, Cervera M. A stabilized formulation for incompressible elasticity using linear displacement and pressure interpolations. *Comput. Methods Appl. Mech. Eng.* 2002; **191**(46):5253–5264.
- [29] Cervera M, Chiumenti M, Valverde Q, Agelet de Saracibar C. Mixed linear/linear simplicial elements for incompressible elasticity and plasticity. *Comput. Methods Appl. Mech. Eng.* 2003; **192**(49–50):5249–5263.

- [30] Chiumenti M, Valverde Q, Agelet de Saracibar C, Cervera M. A stabilized formulation for incompressible plasticity using linear triangles and tetrahedra. *Int. J. Plasticity* 2004; **20**(8–9):1487–1504.
- [31] Codina R. Stabilization of incompressibility and convection through orthogonal sub-scales in finite element methods. *Comput. Methods Appl. Mech. Eng.* 2000; **190**(13):1579–1599.
- [32] Bonet J, Marriott H, Hassan O. Stability and comparison of different linear tetrahedral formulations for nearly incompressible explicit dynamic applications. *Int. J. Numer. Meth. Eng.* 2001; **50**(1):119–133.
- [33] Bonet J, Burton A. A simple average nodal pressure tetrahedral element for incompressible and nearly incompressible dynamic explicit applications. *Comm. Numer. Meth. Eng.* 1998; **14**(5):437–449.
- [34] Puso MA, Solberg J. A stabilized nodally integrated tetrahedral. *Int. J. Numer. Meth. Eng.* August 2006; **67**(6):841–867.
- [35] Dohrmann CR, Heinstein MW, Jung J, Key SW, Witkowski WR. Node-based uniform strain elements for three-node triangular and four-node tetrahedral meshes. *Int. J. Numer. Meth. Eng.* March 2000; **47**(9):1549–1568.
- [36] Gee MW, Dohrmann CR, Key SW, Wall WA. A uniform nodal strain tetrahedron with isochoric stabilization. *Int. J. Numer. Meth. Eng.* 2009; **78**(4):429–443.
- [37] Stenberg R. A family of mixed finite elements for the elasticity problem. *NM* 1988; **53**(5):513–538.
- [38] Cervera M, Chiumenti M, Codina R. Mixed stabilized finite element methods in nonlinear solid mechanics. Part I: Formulation. *Comput. Methods Appl. Mech. Eng.* 2010; **199**(37–40):2559–2570.
- [39] Cervera M, Chiumenti M, Codina R. Mixed stabilized finite element methods in nonlinear solid mechanics. Part II: Strain localization. *Comput. Methods Appl. Mech. Eng.* 2010; **199**(37–40):2571–2589.
- [40] Cervera M, Chiumenti M, Benedetti L, Codina R. Mixed stabilized finite element methods in nonlinear solid mechanics. Part III: Compressible and incompressible plasticity. *Comput. Methods Appl. Mech. Eng.* 2015; **285**:752–775.
- [41] Chiumenti M, Cervera M, Codina R. A mixed three-field fe formulation for stress accurate analysis including the incompressible limit. *Comput. Methods Appl. Mech. Eng.* 2013; .
- [42] Chiumenti M, Cervera M, Codina R. A mixed three-field fe formulation for stress accurate analysis including the incompressible limit. *Comput. Methods Appl. Mech. Eng.* 2015; **283**:1095–1116.
- [43] Lafontaine NM, Rossi R, Cervera M, Chiumenti M. Explicit mixed strain-displacement finite element for dynamic geometrically non-linear solid mechanics. *Comput. Mech.* 2015; **55**(3):543–559.
- [44] Aguirre M, Gil AJ, Bonet J, Carreño AA. A vertex centred finite volume jameson–schmidt–turkel (jst) algorithm for a mixed conservation formulation in solid dynamics. *J. Comput. Phys.* 2014; **259**:672–699.
- [45] Gil AJ, Ortigosa R, Bonet J. A computational framework for polyconvex large strain electro-mechanics. *Submitted to Journal of the Mechanics and Physics of Solids* 2014; .

- [46] Lee CH, Gil AJ, Bonet J. Development of a stabilised Petrov–Galerkin formulation for conservation laws in Lagrangian fast solid dynamics. *Comput. Methods Appl. Mech. Eng.* 2014; **268**:40–64.
- [47] Lee CH, Gil AJ, Bonet J. Development of a cell centred upwind finite volume algorithm for a new conservation law formulation in structural dynamics. *Comput. Struct.* 2013; **118**:13–38.
- [48] Trangenstein JA. Second-order Godunov algorithm for two-dimensional solid mechanics. *Comput. Mech.* 1994; **13**:343–359.
- [49] Pember R, Trangenstein JA. Numerical algorithms for strong discontinuities in elastic-plastic solids. *J. Comput. Phys.* 1992; **103**(1):63–89.
- [50] Colella P, Trangenstein J. A higher-order Godunov method for modeling finite deformation in elastic-plastic solids. *Comm. Pure Appl. Math.* 1991; **44**:41–100.
- [51] Trangenstein JA. The riemann problem for longitudinal motion in an elastic-plastic bar. *SJSSC* 1991; **12**:180–207.
- [52] Bonet J, Gil AJ, Ortigosa R. A computational framework for polyconvex large strain elasticity. *Comput. Methods Appl. Mech. Eng.* 2015; **283**:1061–1094.
- [53] Bonet J, Gil AJ, Lee CH, Aguirre M, Ortigosa R. A first order hyperbolic framework for large strain computational solid dynamics. Part I: Total Lagrangian isothermal elasticity. *Comput. Methods Appl. Mech. Eng.* 2015; **283**:689–732.
- [54] Gil AJ, Lee CH, Bonet J, Aguirre M. A stabilised Petrov–Galerkin formulation for linear tetrahedral elements in compressible, nearly incompressible and truly incompressible fast dynamics. *Comput. Methods Appl. Mech. Eng.* 2014; **276**:659–690.
- [55] Shakib F, Hughes TJR. A new finite element formulation for computational fluid dynamics: IX. Fourier analysis of space-time Galerkin/least-squares algorithms. *Comput. Methods Appl. Mech. Eng.* 1991; **87**:35–58.
- [56] Shakib F, Hughes TJR, Johan Z. A new finite element formulation for computational fluid dynamics: X. The compressible Euler and Navier-Stokes equations. *Comput. Methods Appl. Mech. Eng.* 1991; **89**:141–219.
- [57] Hughes TJR, Franca LP, Mallet M. A new finite element formulation for computational fluid dynamics: I. Symmetric forms of the compressible Euler and Navier-Stokes equations and the second law of thermodynamics. *Comput. Methods Appl. Mech. Eng.* 1986; **54**:223–234.
- [58] Hughes TJR, Mallet M, Mizukami A. A new finite element formulation for computational fluid dynamics: II. Beyond SUPG. *Comput. Methods Appl. Mech. Eng.* 1986; **54**:341–355.
- [59] Hughes TJR, Mallet M. A new finite element formulation for computational fluid dynamics: III. The generalized streamline operator for multidimensional advective-diffusive systems. *Comput. Methods Appl. Mech. Eng.* 1986; **58**:305–328.
- [60] Hughes TJR, Mallet M. A new finite element formulation for computational fluid dynamics: IV. A discontinuity-capturing operator for multidimensional advective-diffusive systems. *Comput. Methods Appl. Mech. Eng.* 1986; **58**:329–336.
- [61] Hughes TJR, Franca LP, Mallet M. A new finite element formulation for computational fluid dynamics: VI. Convergence analysis of the generalized SUPG formulation for linear time-dependent multidimensional advective-diffusive systems. *Comput. Methods Appl. Mech. Eng.* 1987; **63**:97–112.

- [62] Hughes TJR, Franca LP, Hulbert GM. A new finite element formulation for computational fluid dynamics: VIII. The Galerkin/least-squares method for advective-diffusive equations. *Comput. Methods Appl. Mech. Eng.* 1989; **73**:173–189.
- [63] Hauke G. Simple stabilizing matrices for the computation of compressible flows in primitive variables. *Comput. Methods Appl. Mech. Eng.* 2001; **190**:6881–6893.
- [64] Hauke G, Hughes TJR. A unified approach to compressible and incompressible flows. *Comput. Methods Appl. Mech. Eng.* 1994; **113**:389–396.
- [65] Hauke G, Hughes TJR. A comparative study of different sets of variables for solving compressible and incompressible flows. *Comput. Methods Appl. Mech. Eng.* 1998; **153**:1–44.
- [66] Aguirre M, Gil AJ, Bonet J, Lee CH. An upwind vertex centred finite volume solver for lagrangian solid dynamics 2015. (to appear).
- [67] Zienkiewicz OC, Rojek J, Taylor RL, Pastor M. Triangles and tetrahedra in explicit dynamic codes for solids. *Int. J. Numer. Meth. Eng.* 1998; **43**(3):565–583.
- [68] Mira P, Pastor M, Li T, Liu X. A new stabilized enhanced strain element with equal order of interpolation for soil consolidation problems. *Comput. Methods Appl. Mech. Eng.* 2003; **192**(37–38):4257–4277.
- [69] Li X, Han X, Pastor M. An iterative stabilized fractional step algorithm for finite element analysis in saturated soil dynamics. *Comput. Methods Appl. Mech. Eng.* 2003; **192**(35–36):3845–3859.
- [70] Pastor M, Quecedo M, Zienkiewicz OC. A mixed displacement-pressure formulation for numerical analysis of plastic failure. *Comput. Struct.* 1997; **62**(1):13–23.
- [71] Pastor M, Zienkiewicz OC, Li T, Xiaoqing L, Huang M. Stabilized finite elements with equal order of interpolation for soil dynamics problems. *Arch. Comput. Meth. Eng.* 1999; **6**(1):3–33.
- [72] Guermond JL, Quartapelle L. On stability and convergence of projection methods based on pressure poisson equation. *International Journal for Numerical Methods in Fluids* 1998; **26**(9):1039–1053.
- [73] Rojek J, Oñate E, Taylor RL. CBS-based stabilization in explicit solid dynamics. *Int. J. Numer. Meth. Eng.* 2006; **66**(10):1547–1568.
- [74] Oñate E, Rojek J, Taylor RL, Zienkiewicz OC. Finite calculus formulation for incompressible solids using linear triangles and tetrahedra. *Int. J. Numer. Meth. Eng.* 2004; **59**(11):1473–1500.
- [75] Guo Y, Ortiz M, Belytschko T, Repetto EA. Triangular composite finite elements. *Int. J. Numer. Meth. Eng.* January 2000; **47**(1–3):287–316.
- [76] Thoutireddy P, Molinari JF, Repetto EA, Ortiz M. Tetrahedral composite finite elements. *Int. J. Numer. Meth. Eng.* February 2002; **53**(6):1337–1351.
- [77] Pires FMA, de Souza Neto EA, de la Cuesta Padilla JL. An assessment of the average nodal volume formulation for the analysis of nearly incompressible solids under finite strains. *Comm. Numer. Meth. Eng.* 2004; **20**(7):569–583.
- [78] Eyck AT, Lew A. Discontinuous Galerkin methods for non-linear elasticity. *Int. J. Numer. Meth. Eng.* 2006; **67**:1204–1243.

- [79] Eyck AT, Celiker F, Lew A. Adaptive stabilization of discontinuous Galerkin methods for nonlinear elasticity: Analytical estimates. *Comput. Methods Appl. Mech. Eng.* 2008; **197**(33–40):2989–3000.
- [80] Eyck AT, Celiker F, Lew A. Adaptive stabilization of discontinuous Galerkin methods for nonlinear elasticity: Motivation, formulation, and numerical examples. *Comput. Methods Appl. Mech. Eng.* 2008; **197**(45–48):3605–3622.
- [81] Eyck AT, Lew A. An adaptive stabilization strategy for enhanced strain methods in non-linear elasticity. *Int. J. Numer. Meth. Eng.* 2010; **81**(11):1387–1416.
- [82] Kabaria H, Lew AJ, Cockburn B. A hybridizable discontinuous Galerkin formulation for non-linear elasticity. *Comput. Methods Appl. Mech. Eng.* 2015; **283**:303–329.
- [83] Taylor RL. A mixed-enhanced formulation tetrahedral finite elements. *Int. J. Numer. Meth. Eng.* 2000; **47**(1–3):205–227.
- [84] Kasper EP, Taylor RL. A mixed-enhanced strain method. Part I: Geometrically linear problems. *Comput. Struct.* 2000; **75**:237–250.
- [85] Kasper EP, Taylor RL. A mixed-enhanced strain method. Part II: Geometrically nonlinear problems. *Comput. Struct.* 2000; **75**:252–260.
- [86] Auricchio F, da Veiga LB, Lovadina C, Reali A. An analysis of some mixed-enhanced finite element for plane linear elasticity. *Comput. Methods Appl. Mech. Eng.* 2005; **194**(27):2947–2968.
- [87] Arnold DN, Winther R. Mixed finite elements for elasticity. *Numer. Math.* 2002; **92**(3):401–419.
- [88] Arnold DN, Winther R. Nonconforming mixed elements for elasticity. *Math. Models Meth. Appl. Sci.* 2003; **13**(3):295–307.
- [89] Arnold DN, Falk RS, Winther R. Differential complexes and stability of finite element methods ii: The elasticity complex. *Compatible Spatial Discretizations: The IMA Volumes in Mathematics and its Applications* 2006; **142**:47–67.
- [90] Arnold DN, Falk RS, Winther R. Mixed finite element methods for linear elasticity with weakly imposed symmetry. *Math. Comp.* 2007; **76**:1699–1723.
- [91] Arnold DN, Falk RS, Winther R. Differential complexes and stability of finite element methods i. the de rham complex. *Compatible Spatial Discretizations: The IMA Volumes in Mathematics and its Applications* 2006; **142**:23–46.
- [92] Scovazzi G. Lagrangian shock hydrodynamics on tetrahedral meshes: A stable and accurate variational multiscale approach. *J. Comput. Phys.* December 2012; **231**(24):8029–8069.
- [93] Ainsworth M, Oden JT. A unified approach to a posteriori error estimation using residual methods. *Numer. Math.* 1993; **65**:23–50.
- [94] Ainsworth M, Oden JT. A posteriori error estimation in finite element analysis. *Comput. Methods Appl. Mech. Eng.* 1997; **142**:1–88.
- [95] Ainsworth M, Oden JT. An a posteriori error estimate for finite-element approximations of the Navier-Stokes equations. *Comput. Methods Appl. Mech. Eng.* 1994; **111**:185–202.
- [96] Cook RD. Improved two-dimensional finite element. *J. Struct. Div.-ASCE* September 1974; **100**(9):1851–1863.

- [97] Scovazzi G, Christon MA, Hughes TJR, Shadid JN. Stabilized shock hydrodynamics: I. A Lagrangian method. *Comput. Methods Appl. Mech. Eng.* 2007; **196**(4–6):923–966.
- [98] Scovazzi G. Stabilized shock hydrodynamics: II. Design and physical interpretation of the SUPG operator for Lagrangian computations. *Comput. Methods Appl. Mech. Eng.* 2007; **196**(4–6):966–978.
- [99] Scovazzi G, Shadid JN, Love E, Rider WJ. A conservative nodal variational multiscale method for Lagrangian shock hydrodynamics. *Comput. Methods Appl. Mech. Eng.* 2010; **199**(49–52):3059–3100.
- [100] Jansen K, Whiting C, Collis SS, Shakib F. A better consistency for low-order stabilized finite-element methods. *Comput. Methods Appl. Mech. Eng.* 1999; **174**:153–170.
- [101] Love E, Scovazzi G. On the angular momentum conservation and incremental objectivity properties of a predictor/multi-corrector method for Lagrangian shock hydrodynamics. *Comput. Methods Appl. Mech. Eng.* September 2009; **198**(41–44):3207–3213.
- [102] Simo JC, Hughes TJR. *Computational Inelasticity, Interdisciplinary Applied Mathematics*, vol. 7. Springer New York, 2000.
- [103] Hartmann S, Neff P. Polyconvexity of generalized polynomial-type hyperelastic strain energy functions for near-incompressibility. *Int. J. Solids Struct.* 2003; **40**:2767–2791.
- [104] Gurtin ME. *An Introduction to Continuum Mechanics*. Academic Press, 1981.
- [105] Bonet J, Wood RD. *Nonlinear Continuum Mechanics for Finite Element Analysis*. 2nd edn., Cambridge University Press, 2008.
- [106] Belytschko T, Liu WK, Moran B. *Nonlinear Finite Elements for Continua and Structures*. J. Wiley & Sons: New York, 2000.